Towards a numerical laboratory for investigations of gravity-wave mean-flow interactions in the atmosphere

Fabienne Schmid *

Institut für Atmosphäre und Umwelt, Goethe Universität Frankfurt am Main, Frankfurt am Main, Germany

Elena Gagarina

Institut für Atmosphäre und Umwelt, Goethe Universität Frankfurt am Main, Frankfurt am Main, Germany

Rupert Klein

FB Mathematik & Informatik, Freie Universität Berlin, Berlin, Germany

Ulrich Achatz

Institut für Atmosphäre und Umwelt, Goethe Universität Frankfurt am Main, Frankfurt am Main, Germany

* *Corresponding author*: Fabienne Schmid, schmid@iau.uni-frankfurt.de

ABSTRACT

Idealized integral studies of the dynamics of atmospheric inertia-gravity waves (IGWs) from their sources in the troposphere (e.g., by spontaneous emission from jets and fronts) to dissipation and mean-flow effects at higher altitudes could contribute to a better treatment of these processes in IGW parameterizations in numerical weather prediction and climate simulation. It seems important that numerical codes applied for this purpose are efficient and focus on the essentials. Therefore a previously published staggered-grid solver for f-plane soundproof pseudo-incompressible dynamics is extended here by two main components. These are 1) a semi-implicit time stepping scheme for the integration of buoyancy and Coriolis effects, and 2) the incorporation of Newtonian heating consistent with pseudo-incompressible dynamics. This heating function is used to enforce a temperature profile that is baroclinically unstable in the troposphere and it allows the background state to vary in time. Numerical experiments for several benchmarks are compared against a buoyancy/Coriolis-explicit third-order Runge-Kutta scheme, verifying the accuracy and efficiency of the scheme. Preliminary mesoscale simulations with baroclinic-wave activity in the troposphere show intensive small-scale wave activity at high altitudes, and they also indicate there the expected reversal of the zonal-mean-zonal winds.

1. Introduction

Inertia gravity waves (IGWs) play a key role in weather and climate through their transfer of energy and momentum from the troposphere to the middle atmosphere (e.g., Holton et al. 1995; Fritts and Alexander 2003; Plougonven and Zhang 2014, and references therein) that is again known to influence the troposphere on seasonal and longer time scales (e.g., Baldwin et al. 2001; Scaife et al. 2012; Kidston et al. 2015; Baldwin et al. 2021; Martin et al. 2021). Due to their small spatial scales they still pose an important parameterization problem, especially in climate simulations but also in numerical weather prediction. Further improvements of IGW parameterizations require deepened understanding of all aspects of the IGW life cycle, from sources to dissipation and the corresponding large-scale flow effects. Measurements are needed for this as well as high-resolution numerical weather simulations using codes that get as close to real nature as possible. In both, however, one tends to be overwhelmed by the details and it is difficult to discriminate between contributing processes. Hence, numerical studies of idealized scenarios, using a hierarchy of models with increasing complexity, are more or less indispensable for providing an additional focus (Held 2005).

A special challenge of IGW dynamics is the multi-scale aspect represented by the interaction between mesoscale IGWs and the synoptic or planetary-scale flow. This often calls for high-resolution numerical weather simulations in large domains. An example is the spontaneous emission of IGWs by jets and fronts, the latter arising in the development of synoptic-scale mid-latitude dynamics. Various numerical studies have considered idealized dynamical systems to investigate this emission mechanism for IGWs and to gain an improved understanding of the underlying physical processes (e.g., O'Sullivan and Dunkerton 1995; Zhang 2004; Wang and Zhang 2007; Plougonven and Snyder 2007; Hien et al. 2018; Kim

et al. 2016; Borchert et al. 2014; Polichtchouk and Scott 2020). An issue such studies are confronted with is that not all of the mesoscale flow can necessarily be interpreted as IGWs. It is rather to be decomposed into an unbalanced part, attributed to IGWs, and a balanced remainder (Vanneste 2013; Plougonven and Zhang 2014, and references therein). However, the least ambiguous access to indications how this decomposition is best to be done, so as to extract the IGW part propagating from the emission region to the IGW dissipation sites, might only be available by an integral model setting encompassing all of the involved altitudes. Similar considerations also apply to other IGW source processes. Moreover, it seems attractive to also keep the geometry and dynamics of the problem as simple as possible, by assuming an f-plane (e.g., because flow decomposition is most straightforward under such conditions), thereby neglecting the effects of meridional dependency of the Coriolis effect (and thereby Rossby waves with nonzero intrinsic frequency) and of topography by intention. Likewise, unless supplemented by meridional sponges, solid-wall boundary conditions in the meridional direction can contribute to unphysical IGW emission (e.g., Hien et al. 2018; Borchert et al. 2014) so that periodic boundaries in both horizontal directions would also be of interest. Finally, while most of the above-mentioned studies of spontaneous IGW emission consider the initial-value problem of the perturbation of a baroclinically unstable large-scale flow, concerns whether the results depend on the chosen initial condition can best be overcome by simulations of repeated baroclinic-wave life cycles due to the permanent re-establishment of baroclinic instability in the troposphere by a heating process mimicking the effect of solar radiation.

In summary, of interest are long integrations, for a wide and deep domain on an f-plane, of a representation of atmospheric dynamics that is as simple as possible while still allowing for IGWs, including the dissipation after anelastic IGW amplitude growth due to the upwards

decrease of atmospheric density. Mid-latitude baroclinic-wave activity in the troposphere is to be maintained by a representation of the effect of solar heating. Because such integrations are quite costly, efficient time stepping can be of substantial help. This is the motivation of the development reported here, of a an algorithm simulating atmospheric dynamics (i) without sound waves but (ii) allowing for heat sources that is (iii) using semi-implicit time stepping.

As for the choice of an appropriate soundproof representation of atmospheric dynamics, the two most commonly used sets of equations retaining the important anelastic growth of wave amplitudes are the anelastic equations (Batchelor 1953; Ogura and Phillips 1962) and the pseudo-incompressible equations (Durran 1989), both of which include a diagnostic divergence constraint. They have been used successfully for baroclinic life cycle experiments (e.g., Smolarkiewicz and Dörnbrack 2008). The pseudo-incompressible equations are an at least slightly more appropriate tool for the investigation of GW generation, propagation, and dissipation, since, as opposed to the anelastic equations, they are valid for flows with large variations of the background stratification and, as shown by Klein (2009) and Achatz et al. (2010), are consistent with the compressible Euler equations to leading order in the Mach number.

Rieper et al. (2013) have developed a pseudo-incompressible flow solver with implicit turbulence model (PincFloit), the design of which is based on a buoyancy-explicit low-storage Runge–Kutta time stepping scheme, integrating a conservative flux form of the pseudo-incompressible equations of Durran (1989) for adiabatic dynamics on a staggered grid. Applications (e.g., in Bölöni et al. 2016; Wei et al. 2019) show the model's utility for the development and validation of robust strategies for the parameterization of sub-grid scale IGWs. However, (i) only adiabatic flows without any kind of heat source (e.g., the effect of

the convergence of GW entropy fluxes or some radiative heating) could be considered and (ii) the explicit time integration of buoyancy effects imposes a stability-related time step constraint that becomes a critical limitation in long simulations of large-domain flows.

An approach towards the inclusion of diabatic effects is offered by O'Neill and Klein (2014). Based on Almgren et al. (2006, 2008) they have constructed a pseudo-incompressible model including the effects of heat exchange due to external sources. In particular, as opposed to Durran (1989), the authors allowed time-dependent variations of the hydrostatic base state in response to the large-scale heat source. By comparison with a fully-compressible model it was shown that the pseudo-incompressible coding framework with time-dependent background state requires less time steps to simulate a given time period, while it is able to accurately capture acoustically balanced compressible solutions.

Moreover, higher numerical efficiency relative to explicit methods can be achieved by fully implicit or semi-implicit numerical time stepping schemes (e.g., Qaddouri et al. 2021; Smolarkiewicz and Margolin 1997; Bonaventura 2000; Giraldo et al. 2013; Benacchio et al. 2014; Benacchio and Klein 2019). These facilitate efficient and stable long time simulations on much larger and deeper domains than their explicit counterparts. To simplify the discretization, perturbation variables representing deviations of the primary flow variables from a given background state are often used in this context (e.g., Restelli and Giraldo 2009; Smolarkiewicz et al. 2014, 2019). Typically, when applying a semi-implicit scheme, the terms in the equations representing lower-frequency components are integrated using an explicit method, while for the higher-frequency modes an implicit integrator is applied. In the application of such methods one should be aware that the improved efficiency comes at the expense of slowing down the fastest moving waves (Simmons et al. 1978). Hence one always has to make sure that these modes do not contribute significantly.

With the motivation and the background described above the plan of the work reported here has been to enhance the efficiency of PincFloit (Rieper et al. 2013) by the implementation of a semi-implicit time stepping scheme for buoyancy and Coriolis effects (supplementing the implicit treatment of acoustic dynamics built into the very construction of the pseudo-incompressible equations), along the lines of Smolarkiewicz and Margolin (1997) and Benacchio and Klein (2019), but adjusted to the staggered grid. Following the approach of Smolarkiewicz et al. (2001) and Prusa et al. (2008), we design the spatial discretization such that the right-hand sides of the differential equations are reformulated in terms of the deviation from a constant analytically balanced ambient state to ensure that geostrophic and hydrostatic equilibria are fulfilled. A formulation of diabatic heating following O'Neill and Klein (2014) has been included directly into the semi-implicit time stepping procedure. The code allows for integrations in deep domains on a doubly periodic f-plane, and a 'baroclinic-wave and IGW life-cycle' setup close to the Held and Suarez (1994) benchmark is provided for, in which a baroclinically unstable troposphere is maintained by thermal relaxation to a zonally symmetric flow that is baroclinically unstable in the troposphere and barotropic higher up.

The article is structured as follows: Section 2 provides a detailed description of the modeling framework. Section 3 validates the code against a suite of two-dimensional benchmarks, and it also describes preliminary three-dimensional test integrations of the baroclinic-wave and IGW life-cycle setup. This is done merely as a proof of concept while applications to investigations of IGW dynamics will have to wait for future studies. A conclusion and brief outline for future work is given in Section 4.

2. Numerical Model

a. System of equations

The simulations are performed by the atmospheric flow solver pincFlow for the dry, inviscid pseudo-incompressible equations (Durran 1989) in flux form (Klein 2009; Rieper et al. 2013) on an f-plane, with Coriolis parameter f, supplemented by diabatic heating. They can be obtained quite directly from the compressible Euler equations in flux form with heating S

$$\frac{\partial \rho \mathbf{v}}{\partial t} + \nabla \cdot (\mathbf{v} \circ \rho \mathbf{v}) = -c_p \rho \theta \nabla \pi - f \mathbf{e}_z \times \rho \mathbf{u} - \rho g \mathbf{e}_z, \tag{1}$$

$$\frac{\partial \rho}{\partial t} + \nabla \cdot (\rho \mathbf{v}) = 0, \tag{2}$$

$$\frac{\partial \rho \theta}{\partial t} + \nabla \cdot (\rho \theta \mathbf{v}) = S, \tag{3}$$

$$\rho \theta = \frac{p_{00}}{R} \pi^{(1-\kappa)/\kappa}, \tag{4}$$

where $\mathbf{u} = (u, v)^T$ and w are the horizontal and vertical components of the total velocity $\mathbf{v}$. The variables ρ, θ and π denote density, potential temperature, and Exner pressure. Furthermore, p_{00} is a constant reference pressure, g the constant gravitational acceleration, c_p the specific heat capacity at constant pressure, R the gas constant for dry air, $\kappa = R/c_p$ the constant ratio between the two, $\mathbf{e}_z$ the vertical unit vector, and $\circ$ denotes the tensor product, and $\times$ the vectorial cross product. So far the model is restricted to the dry atmosphere.

The pseudo-incompressible approximation is obtained by defining a horizontally homogeneous, hydrostatically balanced, and time dependent background atmosphere which is at rest except for a small vertical motion consistent with the slow heating-induced dilatation of the gas. Thermodynamic fields $\big(\overline{\rho}(t,z), \overline{\theta}(t,z), \overline{P}(t,z), \overline{\pi}(t,z)\big)$ characterize this background state and it is assumed that the mass-weighted potential temperature satisfies

$P = \rho\theta = \overline{P}(t, z)$, so that

$$\rho\theta = P = \overline{P} = \overline{\rho}\overline{\theta}, \tag{5}$$

replaces (4) as the equation of state. A prognostic equation for $\overline{P}$ is then given by the horizontal mean of (3)

$$\frac{\partial \overline{P}}{\partial t} + \frac{\partial \overline{P}\langle w\rangle}{\partial z} = \langle S\rangle, \tag{6}$$

where $\langle \ldots \rangle$ denotes the horizontal mean. Subtracting this from (3) yields the divergence constraint

$$\nabla \cdot \left[\overline{P}(\mathbf{v} - \langle w\rangle \mathbf{e}_z)\right] = S - \langle S\rangle, \tag{7}$$

where, following O'Neill and Klein (2014), the horizontal-mean vertical wind is given by

$$\langle w\rangle(z, t) = \int_{z_0}^{z} \mathrm{d}z' \left(\frac{\langle S\rangle}{\overline{P}} - \frac{1}{\gamma\overline{p}} \frac{d\overline{p}^{top}(t)}{dt} \right), \tag{8}$$

with $z_0 = 0$ the ground altitude, $\overline{p} = p_{00}\overline{\pi}^{1/\kappa}$ the background-atmosphere pressure, and

$$\frac{d\overline{p}^{top}(t)}{dt} = \frac{\int_{z_0}^{H} \mathrm{d}z\, \langle S\rangle / \overline{P}}{\int_{z_0}^{H} \mathrm{d}z\, 1/\gamma\overline{p}} \tag{9}$$

its time derivative at the model top $z = H$. In the absence of heating the background atmosphere would not develop in time. In summary, the pseudo-incompressible system with heating is given by

$$\frac{\partial \rho\mathbf{v}}{\partial t} + \nabla \cdot (\mathbf{v} \circ \rho\mathbf{v}) = -c_p \overline{P} \nabla\pi - f\mathbf{e}_z \times \rho\mathbf{u} - \rho g \mathbf{e}_z, \tag{10}$$

$$\frac{\partial \rho}{\partial t} + \nabla \cdot (\rho\mathbf{v}) = 0, \tag{11}$$

$$\frac{\partial \overline{P}}{\partial t} + \frac{\partial \overline{P}\langle w\rangle}{\partial z} = \langle S\rangle, \tag{12}$$

$$\nabla \cdot (\overline{P}(\mathbf{v} - \langle w\rangle \mathbf{e}_z)) = S - \langle S\rangle, \tag{13}$$

$$\rho\theta = \overline{P}, \tag{14}$$

where (8) defines the horizontal-mean vertical wind. Exner pressure is not determined by the equation of state but by the divergence constraint (13) (as usual for sound-proof/incompressible models). This amounts to an implicit treatment of pressure, and this filters out all acoustic waves. A more detailled description about how the Exner pressure is reconstructed from the other fields is given in Section 2f (i.e., eq. 68). Furthermore, it is worthwhile to mention the equivalence in the pseudo-incompressible model of a conservative density update and the advection of the inverse potential temperature (see Klein 2009).

b. Boundary layer drag and sponge layer

We have extended the system of equations by Rayleigh damping terms, which relax the numerical solution towards a prescribed horizontal wind field $\mathbf{v}_{eq} = (u_{eq}, 0, 0)^T$ assumed to be in geostrophic balance. Hence the momentum equation is supplemented as

$$\frac{\partial \rho \mathbf{v}}{\partial t} + \ldots = \ldots - \alpha_{\mathbf{v}}(z)\rho(\mathbf{v} - \mathbf{v}_{eq}), \tag{15}$$

with the coefficients $\alpha_{\mathbf{v}} = (\alpha_u, \alpha_v, \alpha_w)^T$ for the three momentum components. Near the ground, we use height-dependent Rayleigh drag coefficients adopting the damping profile for the horizontal coefficients from Held and Suarez (1994)

$$\alpha_u(z) = \alpha_v(z) = \frac{1}{\tau_b}\max\left(0, \frac{\sigma - \sigma_b}{1 - \sigma_b}\right), \tag{16}$$

and $\alpha_w(z) = 0$. This serves as a model for boundary layer mixing, where σ_b defines the vertical extent of the mixing in the boundary layer, where τ_b is a minimal damping time scale and $\sigma = {\pi_r}^{\gamma/(\gamma-1)}$ is the normalized background-atmosphere pressure, decreasing from 1 to zero with altitude. By contrast, in the upper domain the damping terms act as a sponge layer that prohibits spurious wave reflections near the model top and the profiles of the three

coefficients in the upper domain are based on Klemp and Lilly (1978)

$$\alpha_u(z) = \alpha_v(z) = \alpha_w(z) = \frac{\alpha_{max}}{\Delta t}\sin^2\left(\frac{\pi}{2}\frac{z - z_s}{H - z_s}\right), \quad \text{if} \quad z_s \leq z \leq H. \tag{17}$$

Here z_s is the altitude of the lower edge of the sponge layer and the parameter α_{max} defines together with the time step Δt the maximum strength of the vertical damping at the model top.

c. Balanced ambient state

The construction of the ambient state in geostrophic balance is based on a prescribed temperature field that is very similar to the radiative temperature distribution by Held and Suarez (1994), and that is given by

$$T_{eq}(y, z) = \max\left\{T_s, \left[\theta_{ref} - \Delta\theta_y\, \mathrm{s}(y) - \frac{\Delta\theta_z}{2}\frac{\gamma}{\gamma - 1}\log(\pi_{eq})\right]\pi_{eq}\right\}, \tag{18}$$

where T_s and θ_{ref} are the stratospheric reference temperature and the surface potential temperature in the tropical troposphere, respectively, $\Delta\theta_y$ the tropospheric potential temperature difference between tropics and poles, and $\Delta\theta_z$ quantifies the stratification of the troposphere. This way the temperature field is baroclinic in the troposphere but constant higher up. Exner pressure and potential temperature are obtained by integrating hydrostatic balance upwards from the ground

$$\frac{\partial \pi_{eq}}{\partial z} = -\frac{g}{c_p \theta_{eq}}, \quad \text{with} \quad \theta_{eq} = \frac{T_{eq}}{\pi_{eq}}, \tag{19}$$

where we assume $\pi_{eq}(z_0) = 1$. Note that in order to avoid numerical instabilities near the upper boundary of the domain, we reduce the Exner pressure within the sponge layer via

$$\pi_{eq} = \begin{cases} \pi_r + (\pi_{eq} - \pi_r)\cos^2\left(\frac{\pi}{2}\frac{z - z_s}{z_s + (H - z_s)/2 - z_s}\right), & \text{if} \quad z_s \leq z \leq z_s + \frac{H - z_s}{2}, \\ \pi_r, & \text{if} \quad z > z_s + \frac{H - z_s}{2}, \end{cases} \tag{20}$$

and afterwards determine a corrected equilibrium potential temperature θ_{eq} from $\partial\pi_{eq}/\partial z$, using (19). Moreover, note that unlike Held and Suarez (1994), $\Delta\theta_z$ is not modulated by a latitude dependence, to avoid small-scale convection near the outer lateral boundaries of the domain. In addition to that, a narrower baroclinic zone is used, such that we define the modification of the horizontal potential temperature gradient $\Delta\theta_y$ as a function of latitude by (see Fig. 1)

$$\mathrm{s}(y) = \begin{cases} 1, & \text{if} \quad y < y_s - \frac{\delta_{jet}}{2}, \\ \sin^2\left(\frac{\pi}{2}\frac{y-(y_s+\delta_{jet}/2)}{\delta_{jet}}\right), & \text{if} \quad y_s - \frac{\delta_{jet}}{2} \le y < y_s + \frac{\delta_{jet}}{2}, \\ 0, & \text{if} \quad y_s + \frac{\delta_{jet}}{2} \le y < y_n - \frac{\delta_{jet}}{2}, \\ \sin^2\left(\frac{\pi}{2}\frac{y-(y_n-\delta_{jet}/2)}{\delta_{jet}}\right), & \text{if} \quad y_n - \frac{\delta_{jet}}{2} \le y < y_n + \frac{\delta_{jet}}{2}, \\ 1, & \text{if} \quad y \ge y_n + \frac{\delta_{jet}}{2}, \end{cases} \tag{21}$$

where $y_{n,s} = \pm L_y/4$ are the positions of two jets in a model domain with meridional extent L_y so that $-L_y/2 \le y \le L_y/2$, and δ_{jet} is a length scale describing the width of the jets. The prescribed wind field is constructed using the geostrophic wind equation

$$u_{eq} = -\frac{1}{f} c_p \theta_{eq} \frac{\partial \pi_{eq}}{\partial y}, \quad \text{and} \quad v_{eq} = w_{eq} = 0. \tag{22}$$

d. Heating function

In our modeling framework the resolved-scale heat source is represented by a simple Newtonian relaxation of the potential temperature field towards the equilibrium distribution defined above

$$S = -\frac{\rho\left[\theta - \theta_{eq}(y,z)\right]}{\tau(y,z)}, \tag{23}$$

where, inspired by Held and Suarez (1994), we use a meridionally-dependent strength of the damping relaxation rate with strong relaxation in the center of the domain and weak relaxation at the lateral boundaries, respectively, given by

$$\tau(y,z) = \frac{1}{\tau_a} + \left(\frac{1}{\tau_s} - \frac{1}{\tau_a}\right) \max\left(0, \frac{\sigma - \sigma_b}{1-\sigma_b}\right) \mathrm{c}(y) \tag{24}$$

with (see Fig. 1)

$$\mathrm{c}(y) = \begin{cases} 0, & \text{if} \quad y < y_s - \frac{\delta_{jet}}{2}, \\ \cos^4\left(\frac{\pi}{2}\frac{y-(y_s+\delta_{jet}/2)}{\delta_{jet}}\right), & \text{if} \quad y_s - \frac{\delta_{jet}}{2} \le y < y_s + \frac{\delta_{jet}}{2}, \\ 1, & \text{if} \quad y_s + \frac{\delta_{jet}}{2} \le y < y_n - \frac{\delta_{jet}}{2}, \\ \cos^4\left(\frac{\pi}{2}\frac{y-(y_n-\delta_{jet}/2)}{\delta_{jet}}\right), & \text{if} \quad y_n - \frac{\delta_{jet}}{2} \le y < y_n + \frac{\delta_{jet}}{2}, \\ 0, & \text{if} \quad y \ge y_n + \frac{\delta_{jet}}{2}. \end{cases} \tag{25}$$

Here τ_a and τ_s are the maximum and minimum relaxation times.

e. Boundary conditions and parameter values

For our needs, we use doubly-periodic boundary conditions in the horizontal to exclude side-wall effects by construction (Hien et al. 2018) and the velocity deviations from the zonally symmetric balanced state (i.e., $[\mathbf{u} - \mathbf{u}_{eq}]$) satisfies free-slip and no-normal flow conditions. Moreover, the vertical derivative of the Exner pressure deviations from π_{eq} as well as the density fluctuations vanish at the vertical boundaries. In closing the description of our numerical model, Table 3 summarizes the constant physical parameters needed in the calculations.

f. Numerical solution procedure

1) Stability related time step constraints

In the implementation by Rieper et al. (2013) of the pseudo-incompressible equations without heating the time integration over a time step Δt utilizes the explicit low-storage third-order Runge-Kutta method of Williamson (1980) for the advection and buoyancy terms, with the time integration step chosen adaptively using the minimum of the time steps computed from various stability criteria. In particular, the scheme includes a stability preserving upper bound of the time step that is given by the inverse of the Brunt-Väisälä frequency. Although this approach works quite well, it becomes increasingly expensive for studies requiring simulations of larger domains and over longer time periods.

In order to achieve higher efficiency, we have implemented a semi-implicit scheme for the time integration of the buoyancy and Coriolis effects together with the pressure terms, that is constructed based on key ideas from Smolarkiewicz and Margolin (1997), and is along the lines of the schemes for the compressible, hydrostatic, and pseudo-incompressible model equations described by Benacchio and Klein (2019). The latter highlighted in a suite of benchmark test cases the schemes' ability to run stably with large time steps, which are dynamically adapted to satisfy only the advection Courant number ν

$$\Delta t_{CFL} = \nu \, \min\left(\frac{\Delta x}{u_{max}}, \frac{\Delta y}{v_{max}}, \frac{\Delta z}{w_{max}}\right), \tag{26}$$

with $u_{max} = \max \mid u \mid$, for instance, and Δx, Δy, and Δz defining a grid cell with grid points fixed and uniformly distributed in x-, y- and z-direction, respectively. We adjusted the scheme to our staggered grid (see Section 2g for details on the spatial discretization) and included numerical aspects from O'Neill and Klein (2014) for the time evolution of the background state. In the following we describe the time stepping procedure.

2) Auxiliary buoyancy related perturbation variable and diabatic pseudo-incompressible equations

For a numerically stable integration with relatively large time steps, the implementation of the semi-implicit time stepping scheme is, in a similar manner to Benacchio and Klein (2019), prepared by introducing an evolution equation for an auxiliary perturbation variable that is representative for buoyancy. For this purpose, a steady, horizontally homogeneous, and hydrostatically balanced *reference atmosphere* at rest is introduced that is not identical with the background atmosphere, although it should be relatively similar. We define $\chi = 1/\theta = \rho/\overline{P}$ and note that the right-hand-side of the vertical momentum equation in (10) can be written as

$$-\overline{P}\left(c_p\frac{\partial\pi}{\partial z}+\chi g\right). \tag{27}$$

Hence a reference atmosphere, indicated by the index r, is in hydrostatic balance if it satisfies

$$0 = -c_p\frac{\mathrm{d}\pi_r}{\mathrm{d}z}-\chi_r g. \tag{28}$$

Defining $\pi' = \pi - \pi_r(z)$ and $\chi' = \chi - \chi_r(z)$ the right-hand side of the vertical momentum equation can therefore also be written as

$$-\overline{P}\left(c_p\frac{\partial\pi}{\partial z}+\chi g\right) = -\overline{P}\left(c_p\frac{\partial\pi'}{\partial z}+\chi' g\right) = -c_p\overline{P}\frac{\partial\pi'}{\partial z}-\rho' g, \tag{29}$$

with a density perturbation

$$\rho' = \overline{P}\chi' = \overline{P}\left(\frac{1}{\theta}-\frac{1}{\theta_r}\right) = \rho - \rho_r\frac{\overline{P}}{P_r}, \tag{30}$$

and in the horizontal momentum equation, with ∇_h the horizontal nabla operator we can replace $-c_p\overline{P}\nabla_h\pi = -c_p\overline{P}\nabla_h\pi'$. Moreover, using $\rho = \overline{P}\chi$, the continuity equation is split

$$\begin{aligned} 0 &= \frac{\partial}{\partial t}\left[\overline{P}\left(\chi_r + \chi'\right)\right] + \nabla\cdot\left[\overline{P}\mathbf{v}\left(\chi_r + \chi'\right)\right] \\ &= \frac{\partial\overline{P}\chi'}{\partial t} + \nabla\cdot\left(\overline{P}\mathbf{v}\chi'\right) + \chi_r\left[\frac{\partial\overline{P}}{\partial t} + \nabla\cdot\left(\overline{P}\mathbf{v}\right)\right] + \overline{P}w\frac{d\chi_r}{dz}, \end{aligned} \tag{31}$$

leading to the auxiliary equation for the density fluctuations

$$\frac{\partial\rho'}{\partial t} + \nabla\cdot\left(\mathbf{v}\rho'\right) = -\frac{\rho_r}{\overline{P}_r}S + w\frac{\overline{P}}{\overline{P}_r}\frac{\rho_r}{g}N^2, \tag{32}$$

with

$$N^2 = \frac{g}{\theta_r}\frac{\mathrm{d}\theta_r}{\mathrm{d}z} \tag{33}$$

the squared Brunt-Väisälä frequency of the reference atmosphere. In summary, including Rayleigh-damping towards an equilibrium horizontal wind, the governing equations forming the basis of our diabatic pseudo-incompressible model with semi-implicit time-stepping scheme read

$$\frac{\partial\rho\mathbf{u}}{\partial t} + \nabla\cdot\left(\mathbf{v}\circ\rho\mathbf{u}\right) = -c_p\overline{P}\nabla_h\pi' - f\mathbf{e}_z\times\rho\mathbf{u} - \alpha_{\mathbf{u}}\rho\left(\mathbf{u}-\mathbf{u}_{eq}\right), \tag{34}$$

$$\frac{\partial\rho w}{\partial t} + \nabla\cdot\left(\mathbf{v}\circ\rho w\right) = -c_p\overline{P}\frac{\partial\pi'}{\partial z} - \rho' g - \alpha_w\rho w, \tag{35}$$

$$\frac{\partial\rho}{\partial t} + \nabla\cdot\left(\rho\mathbf{v}\right) = 0, \tag{36}$$

$$\frac{\partial\rho'}{\partial t} + \nabla\cdot\left(\rho'\mathbf{v}\right) = -\frac{\rho_r}{\overline{P}_r}S + w\frac{\overline{P}}{\overline{P}_r}\frac{\rho_r}{g}N^2, \tag{37}$$

$$\frac{\partial\overline{P}}{\partial t} + \frac{\partial\overline{P}\langle w\rangle}{\partial z} = \langle S\rangle, \tag{38}$$

$$\nabla\cdot\left[\overline{P}(\mathbf{v} - \langle w\rangle\mathbf{e}_z)\right] = S - \langle S\rangle. \tag{39}$$

Obviously the density-perturbation equation (37) is redundant. Note however, that a semi-implicit formulation of the gravity term requires such a split, because it is built upon treating

the advection of the reference-atmosphere potential temperature differently than that of the perturbations. As becoming apparent in the following sections, the reference-atmosphere potential-temperature advection becomes part of the linear operator representing the fast internal wave modes and as such it involves a central discretization in space and the trapezoidal rule in time. This central spatio-temporal discretization would tend to generate unphysical oscillations when applied for the advection of full potential temperature. To make sure such oscillations are suppressed, the advection of perturbation potential temperature is done by the slope-limited explicit second order upwind technology. Nevertheless, since the advection of reference-atmosphere potential temperature is the dominant part of the advection term in many situations, there is still a danger of inducing unwanted oscillations by the central discretization. This is why, in parallel to the splitted scheme, we solve for the advection of full potential temperature with the conservative explicit upwind technology as well. The latter dictates the evolution of full potential temperature over a full time step, whereas the results from the split scheme are used as auxiliary data only in constructing the advective fluxes and in controlling the pseudo-incompressible divergence constraint within the substeps of the semi-implicit scheme. These auxiliary perturbation data are recomputed from the full data at the end of a time step (see eq. 49), such that there are no mass inconsistencies which could result from using different equations for the density and its perturbations.

3) Semi-implicit time discretization

In this section, we provide a compact description of the semi-implicit method adopted for the time discretization of the system (34) - (38), following the presentation of Benacchio and Klein (2019). To this end, using the notation of Smolarkiewicz et al. (2014) and Benacchio

and Klein (2019), we summarize the primary variables in the vector

$$\Psi = (\rho \mathbf{v}, \rho, \rho') \,, \tag{40}$$

and by splitting the equations into advective and non-advective terms, we may write (34) - (37) as

$$\frac{\partial \Psi}{\partial t} + \nabla \cdot (\mathbf{v} \circ \Psi) = Q(\Psi, \overline{P}, \pi'), \tag{41}$$

where $Q(\Psi, \overline{P}, \pi')$ represents the right-hand sides of the prognostic equations (34) - (37).

The main idea of the semi-implicit time integration scheme is treating the advection explicitly using a low-storage Runge-Kutta method of third-order by Williamson (1980), while the remaining terms on the right-hand side of (41) are treated using explicit and implicit Euler steps. Simultaneously, the background state is advanced in time following (38), with $\langle w \rangle$ from (8), and the Exner-pressure fluctuations are determined diagnostically so that the divergence constraint (39) remains satisfied. Since the procedure is closely related to that outlined by Benacchio and Klein (2019), we abbreviate its explanation and only highlight the differences.

The discretization of the time integration over a full time step $t^n \to t^{n+1}$ reads:

- Step 1 and 2:

$$\Psi^{\#} = \Psi^n + A^{\Delta t/2} \left(\Psi^n, (\overline{P}\mathbf{v})^n \right), \tag{42}$$

$$\overline{P}^{n+1/2} = \overline{P}^n - \frac{\Delta t}{2} \left[\left(\frac{(\overline{P}\langle w \rangle)^n_{k+1/2} - (\overline{P}\langle w \rangle)^n_{k-1/2}}{\Delta z} \right) - \langle S \rangle^n \right], \tag{43}$$

$$\Psi^{n+1/2} = \Psi^{\#} + \frac{\Delta t}{2} Q(\Psi^{n+1/2}, \overline{P}^{n+1/2}, \pi'^{n+1/2}). \tag{44}$$

Note that the density is kept constant in (44) because Q does not have an entry in the density component as is seen in (36). The operator A denotes our nonlinear upwind scheme for linear advection of $\Psi/\overline{P}$, with $\overline{P}\mathbf{v}$ prescribed, that uses a third-order

Runge-Kutta time step. The subscripts $(\cdot)_{k\pm1/2}$ denote the vertical position at the upper and lower edge of all scalar cells (see Section 2g below for details). As is outlined further below, the implicit integration of the linear right-hand sides by (44) involves three sub-steps: In a predictor step winds and density (or rather buoyancy) fluctuations are advanced, using the Exner pressure from the previous time step. Via solution of an elliptic equation a new Exner pressure is then diagnosed so that its application in a corrector step leads to wind fields satisfying the divergence constraint (39). Therein, following O'Neill and Klein (2014), the heating term $\langle S \rangle$ and the horizontal-mean vertical wind $\langle w \rangle$, together with the update (43) of the background reflect the presence of heat sources not taken into account by Benacchio and Klein (2019).

- Steps 3-5:

$$\Psi^* = \Psi^n + \frac{\Delta t}{2} Q(\Psi^n, \overline{P}^n, \pi'^n), \tag{45}$$

$$\Psi^{**} = \Psi^* + A^{\Delta t}\left(\Psi^*, (\overline{P}\mathbf{v})^{n+1/2}\right), \tag{46}$$

$$\overline{P}^{n+1} = \overline{P}^n - \Delta t \left[\left(\frac{(\overline{P}\langle w \rangle)^{n+1/2}_{k+1/2} - (\overline{P}\langle w \rangle)^{n+1/2}_{k-1/2}}{\Delta z} \right) - \langle S \rangle^{n+1/2} \right], \tag{47}$$

$$\Psi^{n+1} = \Psi^{**} + \frac{\Delta t}{2} Q(\Psi^{n+1}, \overline{P}^{n+1}, \pi'^{n+1}). \tag{48}$$

Herein (45) is an explicit Euler step for the right-hand sides without adjustment of the Exner pressure and corrector step, while (48) is an implicit time step in line with (44). Finally, we synchronize the density fluctuations by setting

$$\rho'^{,n+1} = \rho^{n+1} - \rho_r \frac{\overline{P}^{n+1}}{P_r}. \tag{49}$$

Note that the present combination of an explicit Euler step at the beginning of the time step and an implicit Euler step at its end corresponds to the trapezoidal rule for time

integration, which is second-order accurate and symplectic. The latter property ensures that the scheme maintains oscillatory behavior induced by the linear terms without damping. The interleaving of these two steps with the advection operator is equivalent to applying the trapezoidal rule along a Lagrangian trajectory (Smolarkiewicz and Margolin 1997; Benacchio and Klein 2019).

There is one caveat in using the trapezoidal rule time integrator for sound-proof models. Because the Exner pressure satisfies a *diagnostic* elliptic equation, it should depend at any given time only on the flow state at that same time, but not on any previous Exner pressure distributions – as would be the case in a compressible flow. The consequence of using the trapezoidal rule time integrator for the momentum equation is, however, that the explicit forward Euler step in (45) adds a contribution to the momentum field that depends on π'^n. If this field includes any deviation, say $\delta\pi$, from the exact pressure solution at time t^n, then the divergence error implied by this contribution has to be corrected in the final step (48), which will therefore deviate from the exact solution at time t^{n+1} by an additional increment $-\delta\pi$. The result is a perpetual oscillation around the correct mean by $\pm\delta\pi$ between subsequent time steps. There are various approaches to avoiding this issue if one is interested in faithful pressure results: One may (i) average the Exner pressure fields between time steps to obtain a pressure at $t^{n+\frac{1}{2}}$ that is void of the spurious oscillation; one may (ii) use the result $\pi'^{n+\frac{1}{2}}$ of the implicit half time step in (44) in place of π'^n in (45) as shown through a careful time level analysis by Chew et al. (2021); or (iii) one may, as we do here, treat pressure in the final step (48) by the implicit Euler discretization over the *full* instead of a half time step. This is detailed further below equation (69). The latter approach formally reduces the scheme to first order in time with respect to Exner pressure, but it effectively damps the

spurious oscillations while otherwise leaving the results unchanged. Nevertheless, note that the practical accuracy of the prognostic fields remains second-order in time (see appendix D).

4) Implicit integration of the linear right-hand sides under consideration of the divergence constraint

The integration of the right-hand sides in (41) is realized by an explicit Euler step without corrector sub-step (i.e., 45), and two implicit Euler steps (i.e., 44 and 48), respectively. Each of the implicit steps consists of a predictor sub-step, then the adjustment of the Exner pressure and finally a corrector sub-step so that the divergence constraint (39) remains satisfied. In this section we outline the essential aspects of all three sub-steps of (44) and (48). Since the continuity equation (11) does not have a right-hand side and the equation to update $\overline{P}$ is not involved in those steps we treat ρ and $\overline{P}$ as well as S as given in the integration of (34), (35) and (37) without advection. Consequently, we may summarize these equations as

$$\frac{\partial \mathbf{v}}{\partial t} = -c_p \frac{1}{\chi^\circ} \nabla \pi' - f \mathbf{e}_z \times \mathbf{u} + b' \mathbf{e}_z - \alpha_{\mathbf{v}} (\mathbf{v} - \mathbf{v}_{eq}), \tag{50}$$

$$\frac{\partial b'}{\partial t} = \frac{\chi_r g}{\rho^\circ} S^\circ - w \frac{\chi_r}{\chi^\circ} N^2, \tag{51}$$

with the buoyancy fluctuations $b' = -g\rho'/\rho^\circ$. Here the superscript $(\cdot)^\circ$ denotes the variables, which are available when the semi-implicit Euler steps are solved. As demonstrated for the example of hydrostatic equilibrium in appendix B, the second-order spatial discretization (see section 2g) on a C-grid to be applied to the right-hand sides is not able to directly respect hydrostatically and geostrophically balanced states in general. To circumvent this problem, we use a strategy which has previously been suggested by Smolarkiewicz et al. (2001) and Prusa et al. (2008). Within this method, we start out with an analytically

balanced state with purely horizontal winds ($w_{eq} = 0$), satisfying

$$0 = -c_p \frac{1}{\chi_{eq}} \nabla \pi'_{eq} - f \mathbf{e}_z \times \mathbf{u}_{eq} + b'_{eq} \mathbf{e}_z, \tag{52}$$

$$0 = \nabla \cdot (\overline{P}_{eq} \mathbf{v}_{eq}). \tag{53}$$

Subtracting (52) from (50) leads to the modified momentum equation

$$\frac{\partial \hat{\mathbf{v}}}{\partial t} \equiv \frac{\partial \mathbf{v}}{\partial t} = -c_p \frac{1}{\chi^\circ} \nabla \hat{\pi}' - c_p \widehat{\left(\frac{1}{\chi^\circ} \right)} \nabla \pi'_{eq} - f \mathbf{e}_z \times \hat{\mathbf{u}} + \hat{b}' \mathbf{e}_z - \alpha_{\mathbf{v}} \hat{\mathbf{v}}, \tag{54}$$

where for any field variable ψ its deviation from the equilibrium field is denoted by $\hat{\psi} = \psi - \psi_{eq}$. The implicit time step for the integration of (54) and (51) is in summary

$$\hat{u}^{n+1} = \hat{u}^n - \Delta t \left[c_p \frac{1}{\chi^\circ} \frac{\partial \hat{\pi}'^{,n+1}}{\partial x} + c_p \widehat{\left(\frac{1}{\chi^\circ} \right)} \frac{\partial \pi'^{,n+1}_{eq}}{\partial x} - f \hat{v}^{n+1} + \alpha_u \hat{u}^{n+1} \right], \tag{55}$$

$$\hat{v}^{n+1} = \hat{v}^n - \Delta t \left[c_p \frac{1}{\chi^\circ} \frac{\partial \hat{\pi}'^{,n+1}}{\partial y} + c_p \widehat{\left(\frac{1}{\chi^\circ} \right)} \frac{\partial \pi'^{,n+1}_{eq}}{\partial y} + f \hat{u}^{n+1} + \alpha_v \hat{v}^{n+1} \right], \tag{56}$$

$$\hat{w}^{n+1} = \hat{w}^n - \Delta t \left[c_p \frac{1}{\chi^\circ} \frac{\partial \hat{\pi}'^{,n+1}}{\partial z} + c_p \widehat{\left(\frac{1}{\chi^\circ} \right)} \frac{\partial \pi'^{,n+1}_{eq}}{\partial z} - \hat{b}'^{,n+1} + \alpha_w \hat{w}^{n+1} \right], \tag{57}$$

$$\hat{b}'^{,n+1} = \hat{b}'^{,n} + \Delta t \left[\frac{\chi_r g}{\rho^\circ} S^\circ - w^{n+1} \frac{\chi_r}{\chi^\circ} N^2 \right]. \tag{58}$$

The Exner pressure is to adjust itself so that the divergence constraint (39) remains satisfied. Hence we split it by $\pi'^{,n+1} = \pi'^{,n} + \delta \pi'^{,n+1}$ into the Exner pressure from the previous time step and an incremental update so that (55) - (58) become

$$u^{n+1} = u^{*,n+1} - \frac{c_p \frac{1}{\chi^\circ} \left[(1 + \alpha_v \Delta t) \frac{\partial \delta \phi'^{,n+1}}{\partial x} + f \Delta t \frac{\partial \delta \phi'^{,n+1}}{\partial y} \right]}{(1 + \alpha_u \Delta t)(1 + \alpha_v \Delta t) + (f \Delta t)^2}, \tag{59}$$

$$v^{n+1} = v^{*,n+1} - \frac{c_p \frac{1}{\chi^\circ} \left[(1 + \alpha_u \Delta t) \frac{\partial \delta \phi'^{,n+1}}{\partial y} - f \Delta t \frac{\partial \delta \phi'^{,n+1}}{\partial x} \right]}{(1 + \alpha_u \Delta t)(1 + \alpha_v \Delta t) + (f \Delta t)^2}, \tag{60}$$

$$w^{n+1} = w^{*,n+1} - \frac{c_p \frac{1}{\chi^\circ} \frac{\partial \delta \phi'^{,n+1}}{\partial z}}{1 + \alpha_w \Delta t + \frac{\chi_r}{\chi^\circ} (N \Delta t)^2}, \tag{61}$$

$$b'^{,n+1} = b'^{*,n+1} + \frac{\frac{\chi_r}{\chi^\circ} N \Delta t^2 c_p \frac{1}{\chi^\circ} \frac{\partial \delta \phi'^{,n+1}}{\partial z}}{1 + \alpha_w \Delta t + \frac{\chi_r}{\chi^\circ} (N \Delta t)^2}, \tag{62}$$

where $\delta\phi' = \Delta t \delta\pi'$, and

$$u^{*,n+1} - u_{eq} = \frac{(1+\alpha_v\Delta t)\left[\hat{u}^n - \Delta t c_p \hat{X}\right] + f\Delta t\left[\hat{v}^n - \Delta t c_p \hat{Y}\right]}{(1+\alpha_u\Delta t)(1+\alpha_v\Delta t) + (f\Delta t)^2}, \tag{63}$$

$$v^{*,n+1} - v_{eq} = \frac{(1+\alpha_u\Delta t)\left[\hat{v}^n - \Delta t c_p \hat{Y}\right] - f\Delta t\left[\hat{u}^n - \Delta t c_p \hat{X}\right]}{(1+\alpha_u\Delta t)(1+\alpha_v\Delta t) + (f\Delta t)^2}, \tag{64}$$

$$w^{*,n+1} - w_{eq} = \frac{\left[w^n - \Delta t c_p \hat{Z}\right] + \Delta t\left[\hat{b}'^{,n} + \Delta t \frac{\chi_r g}{\rho^\circ} S^\circ\right]}{1 + \alpha_w\Delta t + \frac{\chi_r}{\chi^\circ}(N\Delta t)^2}, \tag{65}$$

$$b'^{*,n+1} - b_{eq} = \frac{-\frac{\chi_r}{\chi^\circ}N^2\Delta t\left[w^n - \Delta t c_p \hat{Z}\right] + (1+\alpha_w\Delta t)\left(\hat{b}'^{,n} + \Delta t \frac{\chi_r g}{\rho^\circ} S^\circ\right)}{1 + \alpha_w\Delta t + \frac{\chi_r}{\chi^\circ}(N\Delta t)^2} \tag{66}$$

with again

$$\hat{X}_i = \frac{1}{\chi^\circ}\frac{\partial \hat{\pi}'^{,n}}{\partial x_i} + \widehat{\left(\frac{1}{\chi^\circ}\right)}\frac{\partial \pi'^{,n}_{eq}}{\partial x_i} \tag{67}$$

and x_i any of the three spatial coordinates. The equations (63) - (66) describe the update of wind and buoyancy from the predictor sub-step that uses the Exner pressure from the previous time step. Note that by subtracting geostrophic and hydrostatic equilibrium of a pre-defined state from the right-hand-side momentum equation (50) and thereby obtaining the modified momentum equation (54) one can at least make sure that a predictor sub-step (63) - (66) conserves this single equilibrium state in the absence of heating (so that $S = \langle S \rangle = 0$ and $\langle w \rangle = 0$), and this is also the case after the spatial discretization. We apply this strategy to the balanced ambient state described in section 2c. In the corrector sub-step (59) - (62) the pressure update is taken into account. The final winds must satisfy

the divergence constraint. Hence, inserting (59) - (61) into (39) yields the elliptic equation

$$\begin{aligned}
&\frac{\partial}{\partial x}\left\{\frac{c_p\frac{\overline{P}^{\circ 2}}{\rho^\circ}\left[(1+\alpha_v\Delta t)\frac{\partial\delta\phi',^{n+1}}{\partial x}+f\Delta t\frac{\partial\delta\phi',^{n+1}}{\partial y}\right]}{(1+\alpha_u\Delta t)(1+\alpha_v\Delta t)+(f\Delta t)^2}\right\}\\
&\quad+\frac{\partial}{\partial y}\left\{\frac{c_p\frac{\overline{P}^{\circ 2}}{\rho^\circ}\left[(1+\alpha_u\Delta t)\frac{\partial\delta\phi',^{n+1}}{\partial y}-f\Delta t\frac{\partial\delta\phi',^{n+1}}{\partial x}\right]}{(1+\alpha_u\Delta t)(1+\alpha_v\Delta t)+(f\Delta t)^2}\right\}\\
&\quad+\frac{\partial}{\partial z}\left\{\frac{c_p\frac{\overline{P}^{\circ 2}}{\rho^\circ}\frac{\partial\delta\phi',^{n+1}}{\partial z}}{(1+\alpha_w\Delta t)+\frac{\chi_r}{\chi^\circ}(N\Delta t)^2}\right\}\\
&=\nabla\cdot\left[\overline{P}^\circ(\mathbf{v}^{*,n+1}-\langle w\rangle^\circ\mathbf{e}_z)\right]-(S^\circ-\langle S\rangle^\circ),
\end{aligned}\tag{68}$$

which is solved for the Exner-pressure update, using a preconditioned Bi-Conjugate Gradient STABilized (Bi-CGSTAB) algorithm (Van der Vorst 1992) that stops its iterations once the root-mean-square error between both sides of (68) falls below

$$\begin{aligned}
\epsilon_a=\epsilon_p\Bigg\langle&\left[\frac{\partial}{\partial x}\left(\overline{P}^\circ u^{*,n+1}\right)\right]^2+\left[\frac{\partial}{\partial y}\left(\overline{P}^\circ v^{*,n+1}\right)\right]^2+\left\{\frac{\partial}{\partial z}\left[\overline{P}^\circ\left(w^{*,n+1}-\langle w\rangle^\circ\right)\right]\right\}^2\\
&+(S^\circ-\langle S\rangle^\circ)^2\Bigg\rangle^{1/2}
\end{aligned}\tag{69}$$

with ϵ_p a relative tolerance, and where angular brackets indicate a volume average. This update is then used in the corrector sub-step. Some of the more technical aspects of the used procedure can be found in appendix A. Following Benacchio and Klein (2019), we use a convergence threshold of $\epsilon_p = 10^{-8}$ in the Bi-CGSTAB solver.

Finally note that within (44) the pressure correction (68) is in agreement with the predictor step calculated over half a time step (i.e., $\delta\phi' = (\Delta t/2)\delta\pi'$) so that in the update of the pressure field we use $\pi'^{n+1/2} = \pi'^n + 2\delta\phi'/\Delta t$. This differs, however in (48) where the pressure correction is done over a full time step, since the previous explicit step is determined without a corrector sub-step. Hence $\delta\phi' = \Delta t\delta\pi'$ and therefore $\pi'^{n+1} = \pi'^n + \delta\phi'/\Delta t$.

g. Spatial discretization - general setup

PincFlow uses a standard spatially symmetric second-order accurate finite-volume discretization for the variables on a three-dimensional staggered C-grid (Arakawa and Lamb 1977) with constant side lengths of a grid cell, and $i = 1, \ldots, N_x$, $j = 1, \ldots, N_y$, $k = 1, \ldots, N_z$ indicating the indices of grid cells in zonal, meridional and vertical direction. Thus, the equations are averaged over a grid cell volume $V = \Delta x \Delta y \Delta z$, for instance as

$$\rho^n_{i,j,k} \approx \frac{1}{V} \int_V \rho(x, y, z, t^n) \mathrm{d}V \tag{70}$$

and the scalar variables are indicated by full indices (e.g., $\rho^n_{i,j,k}$) whereas the velocities and momenta are defined at the cell interfaces (e.g., $u^n_{i+1/2,j,k}$, $v^n_{i,j+1/2,k}$, $w^n_{i,j,k+1/2}$).

Following Benacchio et al. (2014) and Benacchio and Klein (2019), we discretize the flux divergences on the left-hand side of equations (34) - (37) by considering $\overline{P}\mathbf{v}$ as the carrier flux (e.g., Klein 2009; Smolarkiewicz et al. 2014, and references therein), meaning that we re-write

$$(\rho\mathbf{v}, \rho'\mathbf{v}) = \left(\overline{P}\mathbf{v}\,\chi, \overline{P}\mathbf{v}\,\chi'\right), \tag{71}$$

$$(\mathbf{v} \circ \rho\mathbf{v}) = \left(\overline{P}\mathbf{v} \circ \chi\mathbf{v}\right). \tag{72}$$

In the original implementation of Rieper et al. (2013) the Adaptive Local Deconvolution Method (ALDM, Hickel et al. 2006) has been used for discretizing the advective fluxes. Although it has been demonstrated that this method provides good results in simulations for several geophysical problems (e.g., Hickel et al. 2006; Remmler and Hickel 2012, 2013; Rieper et al. 2013), benchmark tests by Remmler et al. (2015) against direct numerical simulations have shown that ALDM is in some cases over-dissipative. Thus, in the present implementation we use a Monotone Upwind Scheme for Conservation Laws (MUSCL, see Leer 2006). In appendix C we give a compact description of its key components.

For the integration of the right-hand sides of (50) - (51) we use symmetric second-order accurate differencing in space. We note that by using a staggered Cartesian grid the perturbation Exner pressure is stored at the cell centers instead of at the grid nodes as in Benacchio and Klein (2019). For instance, for the zonal wind the spatial discretization of the corrector sub-step (63) reads

$$u^{n+1}_{i+1/2,j,k} = u^{*,n+1}_{i+1/2,j,k} - \frac{\Delta t c_p \left(\frac{1}{\chi^\circ}\right)_k \left[(1+\alpha_v \Delta t)\frac{\partial \delta\pi'^{,n+1}}{\partial x} + f\Delta t \frac{\partial \delta\pi'^{,n+1}}{\partial y}\right]_{i+1/2,j,k}}{(1+\alpha_{u,k}\Delta t)(1+\alpha_{v,k}\Delta t) + (f\Delta t)^2}, \tag{73}$$

where the zonal Exner-pressure gradient at the chosen u-point is simply

$$\left(\frac{\partial \delta\pi'}{\partial x}\right)_{i+1/2,j,k} = \frac{\delta\pi'_{i+1,j,k} - \delta\pi'_{i,j,k}}{\Delta x}, \tag{74}$$

while the meridional gradient is obtained from those at the v-points by linear interpolation, such that

$$\begin{aligned}\left(\frac{\partial \delta\pi'}{\partial y}\right)_{i+1/2,j,k} =& \frac{1}{4}\Bigg[\left(\frac{\partial \delta\pi'}{\partial y}\right)_{i,j-1/2,k} + \left(\frac{\partial \delta\pi'}{\partial y}\right)_{i,j+1/2,k} \\ &+ \left(\frac{\partial \delta\pi'}{\partial y}\right)_{i+1,j-1/2,k} + \left(\frac{\partial \delta\pi'}{\partial y}\right)_{i+1,j+1/2,k}\Bigg]\end{aligned} \tag{75}$$

with

$$\left(\frac{\partial \delta\pi'}{\partial y}\right)_{i,j+1/2,k} = \frac{\delta\pi'_{i,j+1,k} - \delta\pi'_{i,j,k}}{\Delta y}. \tag{76}$$

The same linear interpolation is also applied to all other instances where winds, buoyancy and Exner-pressure gradients are not directly available at locations of interest. This also holds for the vertical direction. Finally, in its spatial discretization the Exner-pressure equation (68) is evaluated at the scalar points, so that one determines

$$\begin{aligned}\nabla \cdot (\overline{P}^\circ \mathbf{v}^{*,n+1}) \,|_{i,j,k} =& \overline{P}^\circ_k \frac{u^{*,n+1}_{i+1/2,j,k} - u^{*,n+1}_{i-1/2,j,k}}{\Delta x} + \overline{P}^\circ_k \frac{v^{*,n+1}_{i,j+1/2,k} - v^{*,n+1}_{i,j-1/2,k}}{\Delta y} \\ &+ \frac{\overline{P}^\circ_{k+1/2} w^{*,n+1}_{i,j,k+1/2} - \overline{P}^\circ_{k-1/2} w^{*,n+1}_{i,j,k-1/2}}{\Delta z}.\end{aligned} \tag{77}$$

The same locations in the differencing of the winds are also used on the right-hand side of the Exner-pressure equation in (68) for differencing the terms in the square brackets.

3. Model evaluation

a. Standard test cases

To validate the accuracy and efficiency of our semi-implicit method, we use three two-dimensional Cartesian test cases of dry atmospheric dynamics, drawing on the suite considered in Benacchio and Klein (2019). The first test case considers a falling cold air bubble (Straka et al. 1993) to validate the stability and accuracy of the model. Because the test case involves potential temperature diffusion, supplementing the right-hand side of the entropy equation, it is diabatic and hence offers a first possibility to validate the implementation of the heat source together with the corresponding dynamics of the background state. In particular, the results of the semi-implicit model are compared to simulations with a third-order Runge-Kutta scheme as well as with other numerical models from the literature (i.e., Straka et al. 1993; Giraldo and Restelli 2008; Benacchio and Klein 2019; Melvin et al. 2019). To further demonstrate the agreement between our gravity-implicit pseudo-incompressible model pincFlow and a buoyancy-explicit diabatic pseudo-incompressible model, we construced another test case, which includes a stronger heating. Within this second test case, a more realistic atmosphere at rest (Rieper et al. 2013) with a heated layer near the ground, based on the heating profile described by Almgren et al. (2006), together with a local region of heating, which is assumed to have the form of a bubble, are considered. The last test consists of the non-hydrostatic IGW case of Skamarock and Klemp (1994) and its extension of larger-scale configurations for GWs by Benacchio and Klein (2019). It is aimed at testing

especially the efficiency of the semi-implicit time stepping scheme. As a benchmark of the efficiency we use the original time stepping scheme used by Rieper et al. (2013) (i.e., a third-order Runge-Kutta scheme which treats buoyancy explicitly). In none of the standard test cases do we use any ambient equilibrium state, and the thermal relaxation in (23) as well as the boundary-layer and sponge-layer drag as defined in (16) and (17) are switched off. The numerical model is coded in FORTRAN and has been parallelized in the two horizontal directions.

1) Density current

For the first test case of a falling cold bubble (Straka et al. 1993), we consider a two-dimensional domain $(x, z) \in [-25.6, 25.6] \times [0, 6.4]\ \mathrm{km}^2$ with a neutrally stratified atmosphere and $\theta_{ref} = 300\,\mathrm{K}$. An initial thermal perturbation

$$T' = \begin{cases} 0\ \mathrm{K}, & \text{if} \quad r < 1, \\ -7.5\,[1 + \cos(\pi r)]\ \mathrm{K}, & \text{if} \quad r > 1, \end{cases} \tag{78}$$

where the radial distance is calculated from

$$r^2 = \left(\frac{x}{x_r}\right)^2 + \left(\frac{z - z_c}{z_r}\right)^2, \tag{79}$$

with $x_r = 4\,\mathrm{km}$, $z_c = 3\,\mathrm{km}$ and $z_r = 2\,\mathrm{km}$, is placed in the horizontal center of the domain. In order to obtain a grid-converged solution for this test case, artificial diffusion is incorporated by supplementing the left-hand side of the momentum equations (34, 35) with an additional term $-\rho\mu\nabla^2\mathbf{v}$ and by using as heat source $S = \rho\mu\nabla^2\theta$, where the viscosity is $\mu = 75\,\mathrm{m}^2\,\mathrm{s}^{-1}$ (Straka et al. 1993). The initial velocity is set to zero. The simulations are run over a total time span of 900 s, with the Courant number ν (eq. 26) set to 0.5. The maximum time step is dependent on the spatial resolution and given by $\Delta t_{max} = 4\ \mathrm{s} \times \Delta x/50\ \mathrm{m}$. Unless

otherwise stated, we use a spatial resolution of 50 m. Because of the symmetrical nature of the test case, we show only plots for the subdomain $[0, 16] \times [0, 5]$ km^2.

Figure 2 shows the evolution of the potential temperature perturbation of the reference setup for this case. Since the bubble is cold, it falls, hits the ground and travels along the ground, forming vortices. Moreover, for comparison we show in Fig. 2 the result at time $t = 900$ s for a model run with buoyancy effects included in the explicit third-order Runge-Kutta time stepping scheme for advection. The average of the difference is of the order of 1.7×10^{-5} K and the relative L^2 and L^∞ errors are of the order 2.5×10^{-3} and 1.3×10^{-3}, respectively, indicating a close conformity of the two schemes. Furthermore, considering the horizontal cross section of the potential temperature perturbation at $z =$ 1200 m and final time for five different resolutions (i.e., 400 m, 200 m, 100 m, 50 m, and 25 m, in Fig. 3) confirms that our model converges with increasing spatial resolution. Note that the small difference between the lines for 50 m and 25 m resolution, especially around $x =$ 13 km, might be a result of the used limiter function in the advection scheme, reducing locally the order of accuracy of the scheme. In order to quantify the importance of the time evolution of the background state required by the heat source, we compare the final maximum thermal perturbation and the front location (i.e., the 1 K value of the potential temperature perturbation) with the literature values of compressible models (Fig. 4). Even though the comparison of our pseudo-incompressible model with results from compressible models is not entirely fair, it is evident that our model with time-dependent background profiles shows an acceptable agreement.

2) Heating profile with a local hot spot

Next, we assume an atmosphere at rest, where we adopt the background from Rieper et al. (2013): a neutrally stratified troposphere with $\theta_{tr} = 300\,\mathrm{K}$, the tropopause set at $z_{tr} = 12\,\mathrm{km}$, and an isothermal stratosphere above with

$$T_{tr} = \theta_{tr}\left(\frac{p_{tr}}{p_{00}}\right)^{\frac{R}{c_p}}, \quad \text{and} \quad p_{tr} = p_{00}\left(\frac{g z_{tr}}{c_p \theta_{tr}}\right), \tag{80}$$

such that the background potential temperature profile above the tropopause reads

$$\overline{\theta} = \theta_{tr}\exp\left[\frac{g}{c_p T_{tr}}(z - z_{tr})\right]. \tag{81}$$

Similar to Almgren et al. (2006), a layer of the atmosphere is heated for 250 s including a local hot spot, such that the heating profile has the structure

$$S = \begin{cases} S_0\left[\cos^2(0.5\pi r) + \exp\left(-\frac{z-z_c}{r_0}\right)^2\right] & \text{if} \quad r \leq 1, \\ S_0\left[\exp\left(\frac{-(z-z_c)^2}{r_0^2}\right)\right] & \text{if} \quad r > 1, \end{cases} \tag{82}$$

with

$$r^2 = \left(\frac{x}{r_0}\right)^2 + \left(\frac{z - z_c}{r_0}\right)^2, \tag{83}$$

and $r_0 = 1\,\mathrm{km}$, $S_0 = 0.235\,\mathrm{kg\,K\,m^{-3}\,s^{-1}}$, and $z_c = 3\,\mathrm{km}$. After the first 250 s the heating is switched off. The domain spans $(x, z) \in [-5, 5] \times [0, 25]\ \mathrm{km}^2$ with a horizontal grid spacing of 80×200 grid points, and the simulations are run over a total time span of 1800 s. Since the advective Courant number (eq. 26), which is set to $\nu = 1/6$, would in the first steps allow for an infinitely large time step, in this test case the time step is calculated via

$$\Delta t = \min(\Delta t_{GW}, \Delta t_{CFL}), \tag{84}$$

with a time step limitation due to gravity wave oscillations (see e.g., Rieper et al. 2013)

$$\Delta t_{GW} = \frac{1}{N}. \tag{85}$$

In Fig. 5 the isolines of the potential temperature and the vertical momentum are shown after 600 s, 1200 s, and 1800 s. Because of the symmetry of the test case, the plots show only results for a half of the domain and reveal the solutions of the buoyancy-explicit diabatic pseudo-incompressible model and pincFlow on the same axes. As the atmosphere is heated, the *bubble-like* hot spot moves vertically upward, deforms and causes at the tropopause perturbations, that travel GW like through stratospheric altitudes. In this text we focus only on a qualitative comparison between the two used time stepping schemes, and note besides very small discrepancies which arise from the unstable nature of the test case, an overall excellent agreement.

3) Gravity waves

In the third test case, we consider a set of IGW test cases, as proposed by Skamarock and Klemp (1994) and extended by Benacchio and Klein (2019). They show the evolution of a potential temperature perturbation given by

$$\theta' = 0.01\ \mathrm{K} \frac{\sin(\pi z/H)}{1 + [(x - x_0)/a]^2}, \tag{86}$$

in a uniformly stratified channel with $N = 0.01\,\mathrm{s}^{-1}$, where $a = 5\,\mathrm{km}$, $H = 10\,\mathrm{km}$, $x_0 = 100\,\mathrm{km}$ and a constant horizontal flow $u = 20\,\mathrm{m\,s}^{-1}$. The two-dimensional domain spans $(x, z) \in [-x_N/2, x_N/2] \times [0, 10]\ \mathrm{km}^2$ with $t \in [0, T_N]$ s, where we consider $x_N = 150\,\mathrm{km}$ and final time $T_N = 3000\,\mathrm{s}$, respectively. In agreement with Benacchio and Klein (2019), we neglect the Coriolis term, use a spatial resolution of $\Delta x = \Delta z = 1\,\mathrm{km}$ and set the advective Courant number to 0.9.

During the simulation the initial potential temperature propagates symmetrically in both x-directions, and due to the horizontal flow, it travels towards the center of the domain (Fig. 6). Our results at final time look quite similar to Melvin et al. (2019) (see Fig. 2

in Melvin et al. 2019). Next, we extend the test case in accordance to Benacchio and Klein (2019) to create two additional IGW tests to study the efficiency of our semi-implicit model. For those test cases we consider $x_N = 3000$ km (24000 km), $\Delta x = 20$ km (160 km), $T_N = 60000$ s (480000 s), $x_0 = 2000$ km (16000 km), and turn on (off) the rotation (i.e., $f \neq 0$ ($f = 0$)), where the Coriolis term in (34) reads in agreement with Benacchio and Klein (2019) as $f\mathbf{e}_z \times \rho(\mathbf{u} - U\mathbf{e}_x)$ with $U = 20\,\mathrm{m\,s^{-1}}$. The corresponding results of our buoyancy-semi-implicit model at final times for those extended cases are shown in Fig. 7. A qualitative comparison to the results shown by Benacchio and Klein (2019) shows an overall good agreement. However, for the hydrostatic inertia–gravity wave test slightly larger values of the potential temperature perturbation in the center of the domain are observed, whereas our results for the planetary-scale gravity wave test case reveal a more symmetrically structure.

Quantitative comparison of the simulations at final times with runs operated using the buoyancy-explicit third-order Runge-Kutta scheme confirm the high efficiency of our semi-implicit model for simulations over long time periods and large domains (Table 1). In particular, in the case of a coarser resolution our semi-implicit model is up to 10 times faster compared to the model with buoyancy-explicit Runge-Kutta scheme. Moreover, the average time step used by our buoyancy-semi-implicit model compare well with those of Benacchio and Klein (2019).

b. Idealized baroclinic-wave and IGW life cycle case

1) Model and simulation setup

We finally give an account of relatively coarse-resolution simulations of the baroclinic-wave and IGW life-cycle setup of the code. This is to be understood as a mere test of

concept while further tuning of the code, simulations at higher resolution, and analysis of the dynamics is left to future studies. The chosen setup is close to the Held and Suarez (1994) benchmark, with relaxation towards the ambient state described in section 2c with a relaxation rate given by equation (24). To ensure that the impact of the small-scale waves in the middle-atmosphere has sufficient time to develop, we simulate a period of 120 days to allow for repeated baroclinic-wave life cycles. The zonal extension of the simulation domain is $L_x = 4200\,\mathrm{km}$, such that we expect it to contain one wavelength of the baroclinic wave. The meridional width of the domain is $L_y = 16\,800\,\mathrm{km}$ and the model top is placed at $H = 150\,\mathrm{km}$. For the experiment we use a horizontal resolution of 50 km and 300 vertical grid levels. The advective Courant number is $\nu = 1/6$, resulting in an average time step of $\Delta t \approx 111\,\mathrm{s}$.

Our zonally symmetric, initial ambient state is illustrated in Fig. 8. It consists of two zonally uniform jets in thermal wind balance with an initial flow $\mathbf{v}_{eq} = (u_{eq}, 0, 0)^T$, constructed from the equilibrium Exner pressure π_{eq} by geostrophic-wind balance. Due to the horizontally periodic boundary conditions the jets are oppositely directed and we exclude topography, ensuring that the GWs in the simulation are generated internally. The maximum zonal wind speed is of about $46\,\mathrm{m\,s^{-1}}$ at $z \approx 11\,\mathrm{km}$ altitude. Note that the ambient state is baroclinic only in the troposphere but barotropic higher up. To trigger the evolution of a baroclinic wave instability in the troposphere, the simulation is initialized by a small-scale perturbation of the initial potential temperature field at the center of the jets and at a height of the tropopause (i.e., z_{tr}) comparable to Kühnlein et al. (2012) and Schemm et al. (2013). The thermal tropopause anomaly with two centers at $(x, y, z) = (L_x/2, \pm L_y/2, z_{tr})$ has an amplitude of $\delta\theta = 0.3\,\mathrm{K}$, a horizontal and vertical extension of $\delta x = \delta y = 10\,\mathrm{km}$ and

$\delta z = 4\,\mathrm{km}$, and reads

$$\theta' = \pm\delta\theta \cos^2(0.5\pi r), \tag{87}$$

where $r = ([(x - L_x/2)/\delta x]^2 + [(y \mp L_y/2)/\delta y]^2 + [(z - z_{tr})/\delta z]^2)^{1/2}$, respectively.

To maintain stability for long-time integrations, it becomes important to control the grid-scale noise in the absence of a dissipative mechanism (e.g., viscosity). We apply an eighth-order Shapiro filter (Shapiro 1970) with a damping time scale of $10\Delta t$ to the deviations from the initially balanced ambient state in the zonal and meridional directions. The filtering procedure is tied into the semi-implicit scheme by applying it after each of the three predictor steps (one explicit and two implicit).

2) Overview of baroclinic and small-scale waves

Figure 9 summarizes in an exemplary manner the simulated baroclinic-wave activity in terms of the potential temperature at $z = 250\,\mathrm{m}$ altitude along with the horizontal wind fields at z_{tr} between day 60 to day 90. Furthermore, we show the filtered horizontal divergence field (i.e., a horizontal Fourier filter is applied to $\nabla_h \cdot \mathbf{u}$ to remove the part with horizontal wavelengths longer than 1000 km) at z_{tr} as a coarse indicator of emitted small-scale wave packets. On day 60 (Fig. 9a) a developing baroclinic wave can be observed, reaching an overturning phase (day 66, Fig. 9b), before it decays (day 72, Fig. 9c) and afterwards begins to grow again. Figs. 9d - 9f show again intensification, decay and re-intensification of the baroclinic wave. This is accompanied by wavy signals in the filtered horizontal divergence that might be attributable to IGWs. In addition, Fig. 11 illustrates the temporal evolution of the deviation of the volume averaged total kinetic energy (TKE) as well as the available

potential energy (APE)

$$\mathrm{TKE} = \frac{1}{L_x L_y z_{tr}} \int_0^{z_{tr}} \mathrm{d}z \int_{-L_y/2}^{L_y/2} \mathrm{d}y \int_0^{L_x} \mathrm{d}x \frac{\overline{\rho}}{2} \parallel \mathbf{v} \parallel^2, \tag{88}$$

$$\mathrm{APE} = \frac{1}{L_x L_y z_{tr}} \int_0^{z_{tr}} \mathrm{d}z \int_{-L_y/2}^{L_y/2} \mathrm{d}y \int_0^{L_x} \mathrm{d}x \frac{\overline{\rho}}{2N^2} b^2, \tag{89}$$

from their initial value at $t = 0\,\mathrm{s}$ in the troposphere. An increase of the APE is associated with an amplitude growth of the baroclinic wave, which starts approximately around day 7, and is then transformed into kinetic energy, confirming the phases of growth and decay during the baroclinic instability process. For the total kinetic energy an overall decay over time can be observed up to day 60. Thereafter, the TKE stays around a equilibrium value, while for the APE we observe a series of repeated growth and then decay of baroclinic-wave activity in the troposphere.

Next, to investigate the impact of the semi-implicit time stepping scheme (with variable, long time-step sizes) on the small-scale wave solutions, we compare the waves from the initial geostropic adjustment, to the potential-temperature perturbation, to those in semi-implicit simulations using a constant, smaller time step and to results from a simulation using the buoyancy-explicit third-order Runge-Kutta scheme. Table 2 summarises the average time step sizes and number of Poisson iterations of the simulations, while Fig. 10 shows the zonally averaged vertical-velocity field at $t = 2.5\,\mathrm{h}$ from the three different simulations. The overall structure of the fields is similar between the three simulations, with excellent agreement in the troposphere and even higher up but well below the sponge at 100km altitude. However, there are also remaining discrepancies close to the sponge. This is most likely because the strength of the sponge scales inversely with the time step so that the simulations using shorter time steps might have too strong a sponge.

A few indications shall be given on the dynamical situation developing in the simulations in the long run. To this end we show in Fig. 12 a vertical cross section of the deviations of the vertical wind from its zonal mean, at $x = 2100\,\mathrm{km}$ on day 120. Moreover, shown in Fig. 13 are the zonal mean of the zonal wind and the potential temperature fields, both averaged over the last 60 days of the simulation, as well as their difference from the initially balanced fields. The vertical wind in Fig. 12 exhibits small-scale fluctuations at higher altitudes that are most likely to some part due to IGWs that might have been emitted from the troposphere. A decomposition of the upper-atmosphere fluctuations by horizontal spatial filtering, with a separation scale of 1000km, and subsequent analysis of the respective contribution of small-scale fluctuations, interpreted as IGWs, and large-scale fluctuations to the Eliassn-Palm-Flux divergence (not shown) demonstrates that IGWs contribute about as much as the larger-scale fluctuations. Higher-resolution simulations might exhibit a more dominant role of the IGW part.

The zonal-mean fields in Fig. 13 are in geostrophic and hydrostatic balance with the zonal-mean and time-mean Exner pressure (not shown). Results in the 'northern' and 'southern' half of the y-domain are statistically symmetric. Remaining asymmetries are taken to be due to truncation errors in the initial conditions and due to the limited sample size. One sees that tropospheric heat transport has reduced the meridional potential-temperature gradient as compared to the prescribed potential temperature θ_{eq} of the balanced ambient state enforced by the potential-temperature relaxation. Most conspicuous, however, is an increase of the potential temperature in low latitudes at high altitudes just below the sponge (above 90km) and reversed jets in mid-latitudes between 50km and 90km altitude. This wind reversal is reminiscent of IGW effects in the real atmosphere. An analysis whether we see the same effect here is beyond the scope of this work. Further analysis of the zonal-mean and time-

mean zonal momentum equation, however, shows relatively strong steady structures in the meridional wind and in the Shapiro-filter contribution just below the sponge that seem to indicate medium-scale IGWs reflected from the lower edge of the sponge. This indicates that in future studies the strength of the sponge should be chosen weaker so that IGWs are absorbed in the sponge instead of being reflected by it, and that higher vertical resolution and/or a turbulence parameterization (replacing the Shapiro filter) might be necessary to allow the IGWs to break and dissipate already below the sponge.

4. Summary and conclusions

The result of our study is a novel modeling framework for diabatic pseudo-incompressible dynamics. This modeling approach allows for efficient mesoscale simulations of idealized tropospheric baroclinic-wave activity including small-scale wave effects at high altitudes. Closely related to the work of O'Neill and Klein (2014), we have complemented the pseudo-incompressible flow solver, originally designed by Rieper et al. (2013) for the simulation of adiabatic non-rotating dynamics on a staggered grid, by a heating function. To that end, the pseudo-incompressible system has been modified to allow for a temporal variation of the background state. Moreover, the efficiency of the flow solver has been enhanced by the implementation of a semi-implicit second-order accurate numerical time-stepping scheme as proposed by Benacchio and Klein (2019) and - to the best of our knowledge - for the first time adapted to a staggered grid. Finally, to ensure geostrophic and hydrostatic equilibrium, on the numerical level, of an analytically balanced ambient state we have adopted the method suggested by Smolarkiewicz et al. (2001) and Prusa et al. (2008) by subtracting this equilibrium from the momentum equation.

For the verification that the new modeling framework is indeed accurate and more efficient we have conducted a series of idealized test cases at different scales. First, with the density current test case proposed by Straka et al. (1993) we have validated stability and accuracy of the code. It has been shown that the simulations of our pseudo-incompressible framework with heat source and time-dependent background state compare well with published results of compressible models. Second, to validate our extension of the model to include a heat source we have considered an atmosphere at rest with a heated layer and a local bubble-like hot spot. A qualitative comparison of the results with simulations using a buoyancy-explicit third-order Runge-Kutta time integration scheme show, besides very small discrepancies which arise from the unstable nature of the test case, an excellent agreement. Third, we have performed a suite of IGW test cases, originally proposed by Skamarock and Klemp (1994) and extended by Benacchio et al. (2014). Those tests focus on the efficiency of our semi-implicit time stepping scheme for buoyancy and Coriolis effects, by comparison to simulations using a buoyancy-explicit third-order Runge-Kutta time integration scheme. In simulations over long time periods with a coarse resolution the semi-implicit model uses an about 70 times longer average time step than the model with buoyancy-explicit scheme, and requires an up to 10 times shorter computation time. In addition, the average time steps used by our semi-implicit model compare well with those published by Benacchio and Klein (2019).

For a test of concept we have also done simulations with the baroclinic-wave and IGW life-cycle setup of the code. There a geostrophically and hydrostatically balanced ambient zonally symmetric state, designed along the lines devised by Held and Suarez (1994) so that it is baroclinically unstable in the troposphere but barotropic higher up, is perturbed so that tropospheric baroclinic instability sets in. Thermal relaxation towards the potential-

temperature field of the balanced ambient state causes repeated baroclinic-wave life cycles in the troposphere. To keep the setting as simple as possible, f-plane dynamics is considered with periodic boundaries in both horizontal directions. The latter also helps avoiding instabilites that tend to arise at lateral boundaries unless lateral sponges are applied. The test simulations with 50 km horizontal resolution have been done in a deep domain, with a sponge above 100 km altitude, so that IGWs can propagate into the initially barotropic middle atmosphere and potentially influence it by their dissipation. The geostrophic adjustment, resulting from the initial perturbation, shows good agreement between simulations with explicit and semi-implicit time stepping. The latter, however, uses a time step that is 11 times longer, with a corresponding gain in efficiency. An integration of this test case over 120 days shows repeated baroclinic-wave activity in the troposphere, accompanied by a wavy small-scale signal in the horizontal divergence that might be attributed to IGWs emitted by the synoptic-scale flow. At higher altitudes we observe a strong small-scale signal in horizontal divergence and vertical wind that could at least in part be due to IGW propagation from the troposphere into higher altitudes. Averaged over the last 60 days of the simulation, upper-atmosphere zonal-mean potential temperature and zonal wind show a strong response. The latter exhibits a wind reversal that is reminiscent of the IGW effect in the real atmosphere. An analysis whether we see the same here is beyond the scope of the present study. We find that the Eliassen-Palm-flux divergence at higher altitudes is to about equal parts due to synoptic-scale and mesoscale waves. The latter might end up having a bigger share in simulations with higher resolution.

Further analysis indicates that in future studies the sponge should be chosen weaker so as to avoid wave reflection at its lower edge. It might also be advisable to replace the Shapiro filter, chosen to remove the smallest-scale activity from the simulation, by a more

physically formulated turbulence parameterization (e.g., a dynamic Smagorinsky model, see Germano et al. 1991; Lilly 1992). It seems that the efficiency gain of the semi-implicit time stepping makes such efforts attractive. One should also note that the statistical symmetry in the setup, between the 'northern' and 'southern' half of the y-domain allows to mirror one part onto the other so that, for instance, 60 days of simulation data amount to 120 days of analysis data. Hence the wide meridional extent of the model domain is not a waste but can be exploited efficiently.

Acknowledgments. The authors thank the German Research Foundation (DFG) for partial support through the research unit Multiscale Dynamics of Gravity Waves (MS-GWaves) and through grants AC 71/8-2, AC 71/9-2, AC 71/10-2, AC 71/11-2, AC 71/12-2, and KL 611/25-1. U.A. acknowledges partial support through grant CRC 181 "Energy transfers in Atmosphere an Ocean", project number 274762653, projects W01 "Gravity-wave parameterization for the atmosphere" and S02 "Improved Parameterizations and Numerics in Climate Models". R.K. acknowledges partial support through grant CRC 1114 "Scaling Cascades in Complex Systems", Project Number 235221301, Project (A02) "Multiscale data and asymptotic model assimilation for atmospheric flows". Calculations for this research were conducted on the supercomputer facilities of the Center for Scientific Computing of the Goethe University Frankfurt. This work also used resources of the Deutsches Klimarechenzentrum (DKRZ) granted by its Scientific Steering Committee (WLA) under Project bb1097.

Data availability statement. The desribed code and simulation data are available from the authors on request.

APPENDIX A

The pressure solver

The near-exponential altitude dependence of $\overline{P}$ and ρ, as well as the near-proportionality with $\overline{\rho}^{-1/2}$ of the velocity-fluctuation amplitudes in deep atmospheres entails a vertical dependence of the right-hand side of the pressure problem (68) and of the coefficients on the left-hand-side that might lead the BiCGStab that we are using as linear-equation solver to put too much weight into the lower layers. In order to avoid this and also take into account the expected vertical dependence of the Exner-pressure fluctuations we have re-formulated the problem as

$$\begin{aligned}
&\frac{\sqrt{\rho^\circ}}{\overline{P}^\circ}\frac{\partial}{\partial x}\left\{\frac{\overline{P}^{\circ 2}}{\rho^\circ}\frac{(1+\alpha_v\Delta t)\frac{\partial}{\partial x}\left(\frac{\sqrt{\rho^\circ}}{\overline{P}^\circ}\tilde{\pi}^{n+1}\right)+f\Delta t\frac{\partial}{\partial y}\left(\frac{\sqrt{\rho^\circ}}{\overline{P}^\circ}\tilde{\pi}^{n+1}\right)}{(1+\alpha_u\Delta t)(1+\alpha_v\Delta t)+(f\Delta t)^2}\right\}\\
&\quad+\frac{\sqrt{\rho^\circ}}{\overline{P}^\circ}\frac{\partial}{\partial y}\left\{\frac{\overline{P}^{\circ 2}}{\rho^\circ}\frac{(1+\alpha_u\Delta t)\frac{\partial}{\partial y}\left(\frac{\sqrt{\rho^\circ}}{\overline{P}^\circ}\tilde{\pi}^{n+1}\right)-f\Delta t\frac{\partial}{\partial x}\left(\frac{\sqrt{\rho^\circ}}{\overline{P}^\circ}\tilde{\pi}^{n+1}\right)}{(1+\alpha_u\Delta t)(1+\alpha_v\Delta t)+(f\Delta t)^2}\right\}\\
&\quad+\frac{\sqrt{\rho^\circ}}{\overline{P}^\circ}\frac{\partial}{\partial z}\left[\frac{\overline{P}^{\circ 2}}{\rho^\circ}\frac{\frac{\partial}{\partial z}\left(\frac{\sqrt{\rho^\circ}}{\overline{P}^\circ}\tilde{\pi}^{n+1}\right)}{(1+\alpha_w\Delta t)+\frac{\chi_r^\circ}{\chi^\circ}(N\Delta t^\circ)^2}\right]\\
&=\frac{\sqrt{\rho^\circ}}{\overline{P}^\circ}\nabla\cdot\left[\overline{P}^\circ(\mathbf{v}^{*,n+1}-\langle w\rangle^\circ\mathbf{e}_z)\right]-(S^\circ-\langle S\rangle^\circ),
\end{aligned}\tag{A1}$$

where $\tilde{\pi}=\delta\phi' c_p\sqrt{\rho^\circ}/\overline{P}^\circ$ are the re-scaled Exner-pressure increments. We rewrite this equation as

$$\mathcal{L}_h(\tilde{\pi})+\mathcal{L}_v(\tilde{\pi})=b \tag{A2}$$

where the left-hand-side operator has been split into its horizontal part, structurally strongly related to a horizontal Laplacian, and its vertical part that is in its properties related to a simple second derivative in vertical direction. For proper convergence the BiCGStab needs a preconditioner which we obtain be integrating the auxiliary equation

$$\frac{d\tilde{\pi}}{d\eta}=\mathcal{L}_h(\tilde{\pi})+\mathcal{L}_v(\tilde{\pi})-b \tag{A3}$$

that converges with $\eta \to \infty$ to the desired solution, provided b does not project onto the null space of the operator, as is made sure by the fact that its horizontal average vanishes. The eigenvalues of the discretized horizontal and vertical operator parts scale with $1/(\Delta x)^2 + 1/(\Delta y)^2$ and $1/(\Delta z)^2$, respectively. In the case of $(\Delta z)^2 \ll (\Delta x)^2 + (\Delta y)^2$ the vertical problem has by far the larger eigenvalues so that the auxiliary equation can be solved most efficiently by the semi-implicit rule

$$(1 - \Delta\eta\mathcal{L}_v)\,(\tilde{\pi}^{m+1}) = (1 + \Delta\eta\mathcal{L}_h)\,(\tilde{\pi}^m) + \Delta\eta b \tag{A4}$$

For the solution of the implicit problem we use the Thomas algorithm for tridiagonal matrices (Isaacson and Keller 1966). The pseudo time-step $\Delta\eta$ must be short enough so that its product with the largest eigenvalue of the horizontal operator is smaller than 1. Hence we choose

$$\Delta\eta = \frac{\gamma}{2/(\Delta x)^2 + 2/(\Delta y)^2} \tag{A5}$$

with a tunable parameter γ. Another tuning parameter is the number M of pseudo time-steps (i.e., preconditioner iterations). Initializing the preconditioner from zero we found that $0.5 \leq \gamma \leq 0.8$ and $2 \leq M \leq 10$ are reasonable choices. In the case of slow convergence of the preconditioned BiCGStab one can help oneself by increasing M. In the case of very large M (i.e., $M \gg 10$) the preconditioned BiCGStab is found to converge within one iteration.

APPENDIX B

Inability of the discretization to allow for basic equilibria

The second-order spatial accuracy of the discretization comes at a prize. It does not directly allow for fundamental equilibria. We demonstrate this at the example of the hydrostatic equilibrium. Without subtraction of a pre-defined equilibrium (and in the absence of

Rayleigh damping) one would obtain as vertical-wind and buoyancy predictors, instead of (65) and (66),

$$w^{*,n+1} = \frac{\left[w^n - \Delta t c_p \frac{1}{\chi^\circ}\frac{\partial \pi'^{,n}}{\partial z}\right] + \Delta t \left[b'^{,n} + \Delta t \frac{\chi_r g}{\rho^\circ} S^\circ\right]}{1 + \frac{\chi_r}{\chi^\circ}(N\Delta t)^2}, \tag{B1}$$

$$b'^{*,n+1} = \frac{-\frac{\chi_r}{\chi^\circ} N^2 \Delta t \left[w^n - \Delta t c_p \frac{1}{\chi^\circ}\frac{\partial \pi'^{,n}}{\partial z}\right] + \left(b'^{,n} + \Delta t \frac{\chi_r g}{\rho^\circ} S^\circ\right)}{1 + \frac{\chi_r}{\chi^\circ}(N\Delta t)^2}. \tag{B2}$$

In hydrostatic equilibrium one has $w = 0$, and the discretization of the vertical wind predictor (B1) reads, in the absence of heating,

$$\frac{1}{2}(b'^{,n+1}_k + b'^{,n+1}_{k+1}) = \frac{c_p}{\chi^\circ_{k+1/2}} \frac{\pi'^{,n+1}_{k+1} - \pi'^{,n+1}_k}{\Delta z}. \tag{B3}$$

Likewise the discretization of the buoyancy predictor (B2) yields

$$b'^{,n+1}_k = \frac{1}{2}\left(\frac{c_p}{\chi^\circ_{k+1/2}} \frac{\pi'^{,n+1}_{k+1} - \pi'^{,n+1}_k}{\Delta z} + \frac{c_p}{\chi^\circ_{k-1/2}} \frac{\pi'^{,n+1}_k - \pi'^{,n+1}_{k-1}}{\Delta z}\right), \tag{B4}$$

leading to

$$b'^{,n+1}_k = \frac{1}{2}(b'^{,n+1}_{k+1} + b'^{,n+1}_{k-1}). \tag{B5}$$

Consequently, only linear buoyancy profiles, such as $b'_k = B_0 + B_1 z_k$ ($B_0, B_1 = $ const.), are possible, which is unsuitable for most atmospheric applications. They arise from the interpolations in the buoyancy predictor und vertical wind predictor. It can be demonstrated that analogous problems emerge in the horizontal wind predictors (i.e., equations 63 and 64) where the interpolations of the winds in the Coriolis term and of the horizontal pressure derivatives prevent a numerical preservation of the geostrophic equilibrium.

APPENDIX C

Details of the advection scheme

A Runge-Kutta sub-step for the advection of density reads

$$\frac{\rho^{n+1}_{i,j,k} - \rho^{n}_{i,j,k}}{\Delta t} = -\frac{1}{\Delta x}\left(A^{\rho,x}_{i+1/2,j,k} - A^{\rho,x}_{i-1/2,j,k}\right) - \frac{1}{\Delta y}\left(A^{\rho,y}_{i,j+1/2,k} - A^{\rho,y}_{i,j-1/2,k}\right) - \frac{1}{\Delta z}\left(A^{\rho,z}_{i,j,k+1/2} - A^{\rho,z}_{i,j,k-1/2}\right), \tag{C1}$$

where the density fluxes (e.g., in x-direction) are obtained by an upwind approach as

$$A^{\rho,x}_{i+1/2,j,k} = (\overline{P}_k u_{i+1/2,j,k})^n \left[\sigma_{u_{i+1/2}} \tilde{\chi}^R_{i,j,k} + (1 - \sigma_{u_{i+1/2}})\tilde{\chi}^L_{i+1,j,k}\right] \tag{C2}$$

with $\sigma_{u_{i+1/2}} = \mathrm{sgn}\left(\overline{P}_k u^n_{i+1/2,j,k}\right)$, and where the reconstructed values of inverse potential temperature at the cell faces are

$$\tilde{\chi}^L_{i,j,k} = \tilde{\chi}^R_{i,j,k} = \chi^n_{i,j,k} \tag{C3}$$

if either $\chi_{i,j,k} = \chi_{i-1,j,k}$ or $\chi_{i,j,k} = \chi_{i+1,j,k}$, and otherwise

$$\tilde{\chi}^L_{i,j,k} = \chi^n_{i,j,k} - \frac{1}{2}\eta\left(\frac{\chi^n_{i+1,j,k} - \chi^n_{i,j,k}}{\chi^n_{i,j,k} - \chi^n_{i-1,j,k}}\right)(\chi^n_{i,j,k} - \chi^n_{i-1,j,k}), \tag{C4}$$

$$\tilde{\chi}^R_{i,j,k} = \chi^n_{i,j,k} + \frac{1}{2}\eta\left(\frac{\chi^n_{i,j,k} - \chi^n_{i-1,j,k}}{\chi^n_{i+1,j,k} - \chi^n_{i,j,k}}\right)(\chi^n_{i+1,j,k} - \chi^n_{i,j,k}). \tag{C5}$$

Here η describes a slope limiting function that is in the simulations of the standard test cases reported here the monotonized-centered variant limiter (e.g., Kemm 2010):

$$\eta(\xi) = \max\left\{0, \min\left[2\xi, (2+\xi)/3, 2\right]\right\}. \tag{C6}$$

Momentum advection is treated likewise. Momentum and the corresponding product between velocity and inverse potential temperature are obtained by linearly interpolating the scalar fields to the velocity points, for instance as

$$(\rho u)^n_{i+1/2,j,k} = \rho^n_{i+1/2,j,k} u^n_{i+1/2,j,k}, \quad \rho^n_{i+1/2,j,k} = \frac{1}{2}(\rho^n_{i,j,k} + \rho^n_{i+1,j,k}), \tag{C7}$$

$$(\chi u)^n_{i+1/2,j,k} = \chi^n_{i+1/2,j,k} u^n_{i+1/2,j,k}, \quad \chi^n_{i+1/2,j,k} = \frac{1}{2}(\chi^n_{i,j,k} + \chi^n_{i+1,j,k}), \tag{C8}$$

and the advecting velocities at the momentum-cell interfaces are also obtained by linear interpolation, such that

$$u^n_{i,j,k} = \frac{1}{2}(u^n_{i+1/2,j,k} + u^n_{i-1/2,j,k}). \tag{C9}$$

With these definitions the Runge-Kutta sub-steps for momentum advection are analogous to (C1)

$$\begin{aligned}\frac{(\rho u)^{n+1}_{i+1/2,j,k} - (\rho u)^n_{i+1/2,j,k}}{\Delta t} = &- \frac{1}{\Delta x}\left(A^{\rho u,x}_{i+1,j,k} - A^{\rho u,x}_{i,j,k}\right) - \frac{1}{\Delta y}\left(A^{\rho u,y}_{i+1/2,j+1/2,k} - A^{\rho u,y}_{i+1/2,j-1/2,k}\right) \\ &- \frac{1}{\Delta z}\left(A^{\rho u,z}_{i+1/2,j,k+1/2} - A^{\rho u,z}_{i+1/2,j,k-1/2}\right),\end{aligned} \tag{C10}$$

where, for instance, the zonal flux of zonal momentum is

$$A^{\rho u,x}_{i,j,k} = (\overline{P}_k u_{i,j,k})^n \left[\sigma_{u_i}(\widetilde{\chi u})^R_{i-1/2,j,k} + (1-\sigma_{u_i})(\widetilde{\chi u}_{i+1/2,j,k})^L\right], \tag{C11}$$

and the reconstructed $\widetilde{\chi u}$ is obtained from χu using (C3) – (C5), applied to χu instead of χ and with the zonal index shifted by 1/2.

APPENDIX D

Convergence study

To evaluate the accuracy in space of pincFlow, we first ran the case of a travelling rotating smooth vortex (Kadioglu et al. 2008) in the two-dimensional domain $(x, y) \in [0, 1]^2$ m^2 (see also Benacchio et al. 2014, for a description of the test case). PincFlow transports the vortex at the right speed, such that the results at $t = 1$, 2 s are in good agreement with the initial configuration (not shown). The error of the prognostic fields (i.e., ρ, u, v) at $t =$ 1 s with respect to the initial data (see Fig. 14) confirm the quadratic rate of error decay with grid refinement in the L_2 and L_∞ norm, confirming the second-order accuracy of the

scheme. In addition, we have performed analogous experiments with the non-hydrostatic IGW test case of Skamarock and Klemp (1994) to evaluate the accuracy of the semi-implicit integration of buoyancy effects in time, and similarly observe a second-order convergence rate with descreasing Δt for the prognostic variables (ρ, u, v). This is shown in Fig. 15.

References

Achatz, U., R. Klein, and F. Senf, 2010: Gravity waves, scale asymptotics and the pseudo–incompressible equations. *J. Fluid Mech.*, **663**, 120–147, doi:10.1017/S0022112010003411.

Almgren, A. S., J. B. Bell, A. Nonaka, and M. Zingale, 2008: Low Mach Number Modeling of Type Ia Supernovae. III. Reactions. *Astrophys. J.*, **684**, 449–470, doi:10.1086/590321.

Almgren, A. S., J. B. Bell, C. A. Rendleman, and M. Zingale, 2006: Low Mach Number Modeling of Type Ia Supernovae. I. Hydrodynamics. *Astrophys. J.*, **637**, 922–936, doi:10.1086/498426.

Arakawa, A., and V. R. Lamb, 1977: Computational design of the basic dynamical processes of the UCLA general circulation model. *Methods Comput. Phys.*, **17**, 173–265.

Baldwin, M. P., and Coauthors, 2001: The quasi–biennial oscillation. *Rev. Geophys.*, **39**, 179–229, doi:10.1029/1999RG000073.

Baldwin, M. P., and Coauthors, 2021: Sudden stratospheric warmings. *Reviews of Geophysics*, **59 (1)**, e2020RG000 708, doi:https://doi.org/10.1029/2020RG000708, URL https://agupubs.onlinelibrary.wiley.com/doi/abs/10.1029/2020RG000708, e2020RG000708 10.1029/2020RG000708, https://agupubs.onlinelibrary.wiley.com/doi/pdf/10.1029/2020RG000708.

841 Batchelor, G., 1953: The conditions for dynamical similarity of motions of a friction-
842 less perfect–gas atmosphere. *Quart. J. Roy. Meteor. Soc.*, **79**, 224–235, doi:10.1002/qj.
843 49707934004.

844 Benacchio, T., and R. Klein, 2019: A Semi–Implicit Compressible Model for Atmospheric
845 Flows with Seamless Access to Soundproof and Hydrostatic Dynamics. *Mon. Wea. Rev.*,
846 **147**, 4221–4240, doi:10.1175/MWR-D-19-0073.1.

847 Benacchio, T., W. P. O'Neill, and R. Klein, 2014: A Blended Soundproof–to–Compressible
848 Numerical Model for Small– to Mesoscale Atmospheric Dynamics. *Mon. Wea. Rev.*, **142**,
849 4416–4438, doi:10.1175/MWR-D-13-00384.1.

850 Bölöni, G., B. Ribstein, J. Muraschko, C. Sgoff, J. Wei, and U. Achatz, 2016: The Inter-
851 action between Atmospheric Gravity Waves and Large–Scale Flows: An Efficient De-
852 scription beyond the Nonacceleration Paradigm. *J. Atmos. Sci.*, **73**, 4833–4852, doi:
853 10.1175/JAS-D-16-0069.1.

854 Bonaventura, L., 2000: A Semi–implicit Semi–Lagrangian Scheme Using the Height Coor-
855 dinate for a Nonhydrostatic and Fully Elastic Model of Atmospheric Flows. *J. Comput.*
856 *Phys.*, **158**, 186–213, doi:10.1006/jcph.1999.6414.

857 Borchert, S., U. Achatz, and M. Fruman, 2014: Gravity wave emission in an atmosphere–
858 like configuration of the differentially heated rotating annulus experiment. *J. Fluid Mech.*,
859 **758**, 287–311, doi:10.1017/jfm.2014.528.

860 Chew, R., T. Benacchio, G. Hastermann, and R. Klein, 2021: A one-step blended
861 soundproof-compressible model with balanced data assimilation: theory and idealised
862 tests. *Mon. Wea. Rev.*, **submitted**, arXiv:2103.11861.

863 Durran, D., 1989: Improving the Anelastic Approximation. *J. Atmos. Sci.*, **46**, 1453–1461,
864 doi:10.1175/1520-0469(1989)046⟨1453:ITAA⟩2.0.CO;2.

865 Fritts, D. C., and M. J. Alexander, 2003: Gravity wave dynamics and effects in the middle
866 atmosphere. *Rev. Geophys.*, **41**, 1003, doi:10.1029/2001RG000106.

867 Germano, M., U. Piomelli, P. Moin, and W. H. Cabot, 1991: A dynamic subgrid-scale eddy
868 viscosity model. *Phys. Fluids A*, **3**, 1760–1765.

869 Giraldo, F. X., J. F. Kelly, and E. M. Constantinescu, 2013: Implicit–explicit formulations of
870 a three-dimensional nonhydrostatic unified model of the atmosphere (NUMA). *SIAM J.*
871 *Sci. Comput.*, **35**, B1162–B1194, doi:10.1137/120876034.

872 Giraldo, F. X., and M. Restelli, 2008: A study of spectral element and discontinuous
873 Galerkin methods for the Navier–Stokes equations in nonhydrostatic mesoscale atmo-
874 spheric modeling: Equation sets and test cases. *J. Comput. Phys.*, **227**, 3849–3877, doi:
875 10.1016/j.jcp.2007.12.009.

876 Held, I., 2005: The Gap between Simulation and Understanding in Climate Modeling. *Bull.*
877 *Amer. Meteor. Soc.*, **86**, 1609–1614, doi:10.1175/BAMS-86-11-1609.

878 Held, I. M., and M. J. Suarez, 1994: A Proposal for the Intercomparison of the Dynamical
879 Cores of Atmospheric General Circulation Models. *Bull. Amer. Meteor. Soc.*, **75**, 1825–
880 1830, doi:10.1175/1520-0477(1994)075⟨1825:APFTIO⟩2.0.CO;2.

881 Hickel, S., N. Adams, and J. Domaradzki, 2006: An adaptive local deconvolution method
882 for implicit LES. *J. Comp. Phys.*, **213**, 413–436, doi:10.1016/j.jcp.2005.08.017.

Hien, S., J. Rolland, S. Borchert, L. Schoon, C. Zuelicke, and U. Achatz, 2018: Spontaneous inertia–gravity wave emission in the differentially heated rotating annulus experiment. *J. Fluid Mech.*, **838**, 5–41, doi:10.1017/jfm.2017.883.

Holton, J. R., P. H. Haynes, M. E. McIntyre, A. R. Douglass, R. B. Road, and L. Pfister, 1995: Stratosphere–troposphere exchange. *Rev. Geophys.*, **22**, 403–439, doi:10.1029/95RG02097.

Isaacson, E., and H. B. Keller, 1966: *Analysis of numerical methods*. Wiley.

Kadioglu, S., R. Klein, and M. Minion, 2008: A fourth-order auxiliary variable projection method for zero-Mach number gas dynamics. *J. Comp. Phys.*, **227**, 2012–2043, doi:10.1016/j.jcp.2007.10.008.

Kemm, F., 2010: A comparative study of TVD-limiters – well-known limiters and an introduction of new ones. *Int. J. Numer. Meth. Fluids*, **67**, 404–440, doi:10.1002/fld.2357.

Kidston, J., A. A. Scaife, S. C. Hardiman, D. M. Mitchell, N. Butchart, M. P. Baldwin, and L. J. Gray, 2015: Stratospheric influence on tropospheric jet streams, storm tracks and surface weather. *Nature Geosci.*, **8 (6)**, 433–440, URL http://dx.doi.org/10.1038/ngeo2424.

Kim, Y.-H., H.-Y. Chun, S.-H. Park, I.-S. Song, and H.-J. Choi, 2016: Characteristics of gravity waves generated in the jet–front system in a baroclinic instability simulation. *Atmos. Chem. Phys.*, **16**, 4799–4815, doi:10.5194/acp-16-4799-2016.

Klein, R., 2009: Asymptotics, structure, and integration of soundproof atmospheric flow equations. *Theor. Comput. Fluid Dyn.*, **23**, 161–195, doi:10.1007/s00162-009-0104-y.

Klemp, J. B., and D. K. Lilly, 1978: Numerical simulation of hydrostatic mountain waves. *J. Atmos. Sci.*, **35**, 78–107, doi:10.1175/1520-0469(1978)035⟨0078:NSOHMW⟩2.0.CO;2.

Kühnlein, C., P. Smolarkiewicz, and P. Dörnbrack, 2012: Modelling atmospheric flows with adaptive moving meshes. *J. Comput. Phys.*, **231**, 2741–2763, doi:10.1016/j.jcp.2014.01.031.

Leer, B. V., 2006: Upwind and high–resolution methods for compressible flow: From donor cell to residual–distribution schemes. *16th AIAA Computational Fluid Dynamics Conf.*, Orlando, FL, American Institute of Aeronautics and Astronautics, AIAA, 2003–3559, https://doi.org/10.2514/6.2003-3559.

Lilly, D. K., 1992: A proposed modification of the Germano subgrid-scale closure method. *Phys. Fluids A*, **4**, 633–635.

Martin, Z., S.-W. Son, A. Butler, H. Hendon, H. Kim, A. Sobel, S. Yoden, and C. Zhang, 2021: The influence of the quasi-biennial oscillation on the madden–julian oscillation. *Nat. Rev. Earth Environ.*, **2**, 477–489, doi:https://doi.org/10.1038/s43017-021-00173-9.

Melvin, T., T. Benacchio, B. Shipway, N. Wood, J. Thuburn, and C. Cotter, 2019: A mixed finite–element, finite-volume, semi–implicit discretization for atmospheric dynamics: Cartesian geometry. *Quart. J. Roy. Meteor. Soc.*, **145**, 2835–2853, doi:10.1002/qj.3501.

Ogura, Y., and N. A. Phillips, 1962: Scale Analysis of Deep and Shallow Convection in the Atmosphere. *J. Atmos. Sci.*, **19**, 173–179, doi:10.1175/1520-0469(1962)019⟨0173:SAODAS⟩2.0.CO;2.

O'Neill, W., and R. Klein, 2014: A moist pseudo–incompressible model. *Atmos. Res.*, **142**, 133–141, doi:10.1016/j.atmosres.2013.08.004.

O'Sullivan, D., and T. J. Dunkerton, 1995: Generation of Inertia–Gravity Waves in a Simulated Life Cycle of Baroclinic Instability. *J. Atmos. Sci.*, **52**, 3695–3716, doi:10.1175/1520-0469(1995)052⟨3695:GOIWIA⟩2.0.CO;2.

Plougonven, R., and C. Snyder, 2007: Inertia–Gravity Waves Spontaneously Generated by Jets and Fronts. Part I: Different Baroclinic Life Cycles. *J. Atmos. Sci.*, **64**, 2502–2520, doi:10.1175/JAS3953.1.

Plougonven, R., and F. Zhang, 2014: Internal gravity waves from atmospheric jets and fronts. *Rev. Geophys.*, **52**, 33–76, doi:10.1002/2012RG000419.

Polichtchouk, I., and R. Scott, 2020: Spontaneous inertia-gravity wave emission from a nonlinear critical layer in the stratosphere. *Quart. J. Roy. Meteor. Soc.*, **146**, 1516–1528, doi:10.1002/qj.3750.

Prusa, J., P. Smolarkiewicz, and A. Wyszogrodzki, 2008: EULAG, a Computational Model for Multiscale Flows. *Computers & Fluids*, **37**, 1193–1207, doi:10.1016/j.compfluid.2007.12.001.

Qaddouri, A., C. Girard, S. Husain, and R. Aider, 2021: Implementation of a Semi-Lagrangian Fully Implicit Time Integration of the Unified Soundproof System of Equations for Numerical Weather Prediction. *Mon. Wea. Rev.*, **149**, 2011–2029, doi:10.1175/MWR-D-20-0291.1.

Remmler, S., and S. Hickel, 2012: Direct and large eddy simulation of stratified turbulence. *Int. J. Heat Fluid Flow*, **35**, 13–24, doi:10.1016/j.ijheatfluidflow.2012.03.009.

947 Remmler, S., and S. Hickel, 2013: Spectral structure of stratified turbulence: direct numeri-
948 cal simulations and predictions by large eddy simulation. *Theor. Comput. Fluid Dyn.*, **27**,
949 319–336, doi:10.1007/s00162-012-0259-9.

950 Remmler, S., S. Hickel, M. Fruman, and U. Achatz, 2015: Validation of large–eddy
951 simulation methods for gravity wave breaking. *J. Atmos. Sci.*, **72**, 3537–3562, doi:
952 10.1175/JAS-D-14-0321.1.

953 Restelli, M., and F. X. Giraldo, 2009: A conservative discontinuous Galerkin semi-implicit
954 formulation for the Navier-Stokes equations in nonhydrostatic mesoscale modeling. *SIAM*
955 *J. Sci. Comput.*, **31**, 2231–2257, doi:10.1137/070708470.

956 Rieper, F., S. Hickel, and U. Achatz, 2013: A Conservative Integration of the Pseudo–
957 Incompressible Equations with Implicit Turbulence Parameterization. *Mon. Wea. Rev.*,
958 **141**, 861–886, doi:10.1175/MWR-D-12-00026.1.

959 Scaife, A., and Coauthors, 2012: Climate change projections and stratosphere-troposphere
960 interaction. *Clim. Dyn.*, **38 (9-10)**, 2089–2097, doi:10.1007/s00382-011-1080-7, URL
961 http://dx.doi.org/10.1007/s00382-011-1080-7.

962 Schemm, S., H. Wernli, and L. Papritz, 2013: Warm Conveyor Belts in Idealized Moist
963 Baroclinic Wave Simulations. *J. Atmos. Sci.*, **70**, 627–652, doi:10.1175/JAS-D-12-0147.1.

964 Shapiro, R., 1970: Smoothing, filtering and boundary effects. *Rev. Geophys.*, **8**, 359–387,
965 doi:10.1029/RG008i002p00359.

966 Simmons, A. J., B. J. Hoskins, and D. M. Burridge, 1978: Stability of the Semi-Implicit
967 Method of Time Integration. *Mon. Wea. Rev.*, **106**, 405–412, doi:10.1175/1520-0493(1978)
968 106⟨0405:SOTSIM⟩2.0.CO;2.

969 Skamarock, W., and J. B. Klemp, 1994: Efficiency and accuracy of the Klemp–Wilhelmson
970 time–splitting technique. *Mon. Wea. Rev.*, **122**, 2623–2630, doi:10.1175/1520-0493(1994)
971 122,2623:EAAOTK.2.0.CO;2.

972 Smolarkiewicz, P., and A. Dörnbrack, 2008: Conservative integrals of adiabatic Durran's
973 equations. *Int. J. Numer. Meth. Fluids*, **56**, 1513–1519, doi:10.1002/fld.1601.

974 Smolarkiewicz, P., C. Kühnlein, and N. Wedi, 2014: A consistent framework for discrete
975 integrations of soundproof and compressible PDEs of atmospheric dynamics. *J. Comput.*
976 *Phys.*, **263**, 185–205, doi:10.1016/j.jcp.2014.01.031.

977 Smolarkiewicz, P., C. Kühnlein, and N. Wedi, 2019: Semi–implicit integrations of pertur-
978 bation equations for all–scale atmospheric dynamics. *J. Comput. Phys.*, **376**, 145–159,
979 doi:10.1016/j.jcp.2018.09.032.

980 Smolarkiewicz, P., and L. G. Margolin, 1997: On forward–in–time differencing for fluids:
981 An Eulerian/semi–Lagrangian non–hydrostatic model for stratified flows. *Atmos.–Ocean*,
982 **35**, 127–157, doi:10.1080/07055900.1997.9687345.

983 Smolarkiewicz, P. K., L. G. Margolin, and A. A. Wyszogrodzki, 2001: A Class of Nonhydro-
984 static Global Models. *J. Atmos. Sci.*, **58**, 349–364, doi:10.1175/1520-0469(2001)058⟨0349:
985 ACONGM⟩2.0.CO;2.

986 Straka, J. M., R. B. Wilhelmson, L. J. Wicker, J. R. Anderson, and K. K. Droegemeier,
987 1993: Numerical solutions of a non–linear density current: A benchmark solution and
988 comparisons. *Int. J. Numer. Methods Fluids*, **17**, 1–22, doi:10.1002/fld.1650170103.

Van der Vorst, H. A., 1992: Bi–CGSTAB: A fast and smoothly converging variant of Bi–CG for the solution of nonsymmetric linear systems. *SIAM J. Sci. and Stat. Comput.*, **13**, 631–644, doi:10.1137/0913035.

Vanneste, J., 2013: Balance and Spontaneous Wave Generation in Geophysical Flows. *Ann. Rev. Fluid Mech.*, **45 (1)**, 147–172, doi:10.1146/annurev-fluid-011212-140730.

Wang, S., and F. Zhang, 2007: Sensitivity of Mesoscale Gravity Waves to the Baroclinicity of Jet–Front Systems. *Mon. Wea. Rev.*, **135**, 670–688, doi:10.1175/MWR3314.1.

Wei, J., G. Bölöni, and U. Achatz, 2019: Efficient Modeling of the Interaction of Mesoscale Gravity Waves with Unbalanced Large–Scale Flows: Pseudomomentum–Flux Convergence versus Direct Approach. *J. Atmos. Sci.*, **76**, 2715–2738, doi:10.1175/JAS-D-18-0337.1.

Williamson, J., 1980: Low–storage Runge–Kutta schemes. *J. Comput. Phys.*, **35**, 48–56, doi:10.1016/0021-9991(80)90033-9.

Zhang, F., 2004: Generation of Mesoscale Gravity Waves in Upper–Tropospheric Jet–Front Systems. *J. Atmos. Sci.*, **61**, 440–457, doi:10.1175/1520-0469(2004)061⟨0440:GOMGWI⟩2.0.CO;2.

LIST OF TABLES

TABLE 1: Comparison of the average time step, run time, and average number of iterations of the Poisson solver for the model with semi-implicit time stepping scheme (SI) and a third-order Runge-Kutta time stepping scheme (RK3) for three different configurations of the IGWs test (Skamarock and Klemp 1994; Benacchio and Klein 2019).

$t_N[s]$	$x_N[km]$	$f[s^{-1}]$	Scheme	$\Delta t[s]$	CPU-time $[s]$	Solver it.
3000	300	0	SI	44.78	22	65
			RK3	44.78	18	57
60000	6000	10^{-4}	SI	895.52	20	57
			RK3	99.67	66	19
480000	48000	0	SI	7164.18	21	61
			RK3	99.73	221	37

TABLE 2: Comparison of the average time step and average number of iterations of the Poisson solver for the model with semi-implicit time stepping scheme (SI) using a variable time-step size, SI using a constant (smaller) time step size and a third-order Runge-Kutta time stepping scheme (RK3) for the idealized baroclinic wave life cycle case during the first 12 h.

Scheme	$\Delta t[s]$	Solver it.
SI	140.26	74
SI	2.28 (= const.)	120
RK3	2.28	6.3

TABLE 3: Fixed physical parameter values used in this study.

Parameter	Value
f	$1 \times 10^{-4}\,\mathrm{s}^{-1}$
g	$9.81\,\mathrm{m\,s}^{-2}$
p_{00}	$1 \times 10^{5}\,\mathrm{Pa}$
R	$287\,\mathrm{J\,K}^{-1}\,\mathrm{kg}^{-1}$
γ	1.4
z_s	100 km
α_{max}	1
τ_a	40 d
τ_s	4 d
τ_b	1 d
σ_b	0.7
L_x	4200 km
L_y	16 800 km
H	150 km
θ_{ref}	315 K
T_s	200 K
$\Delta\theta_z$	20 K
ΔT_y	30 K
δ_{jet}	4200 km
z_{tr}	11.25 km

LIST OF FIGURES

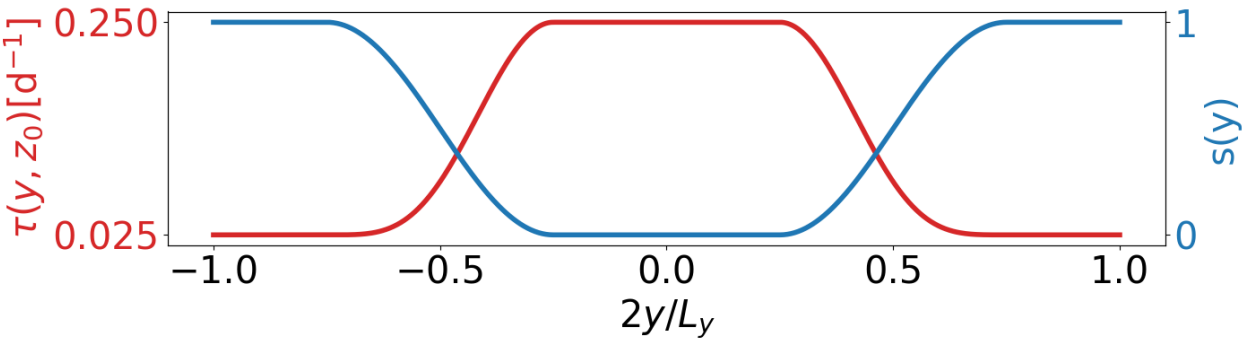

FIG. 1: Meridional distribution of the damping relaxation rate (red, eq. 24) and meridional modification function for ΔT_y (blue, eq. 21).

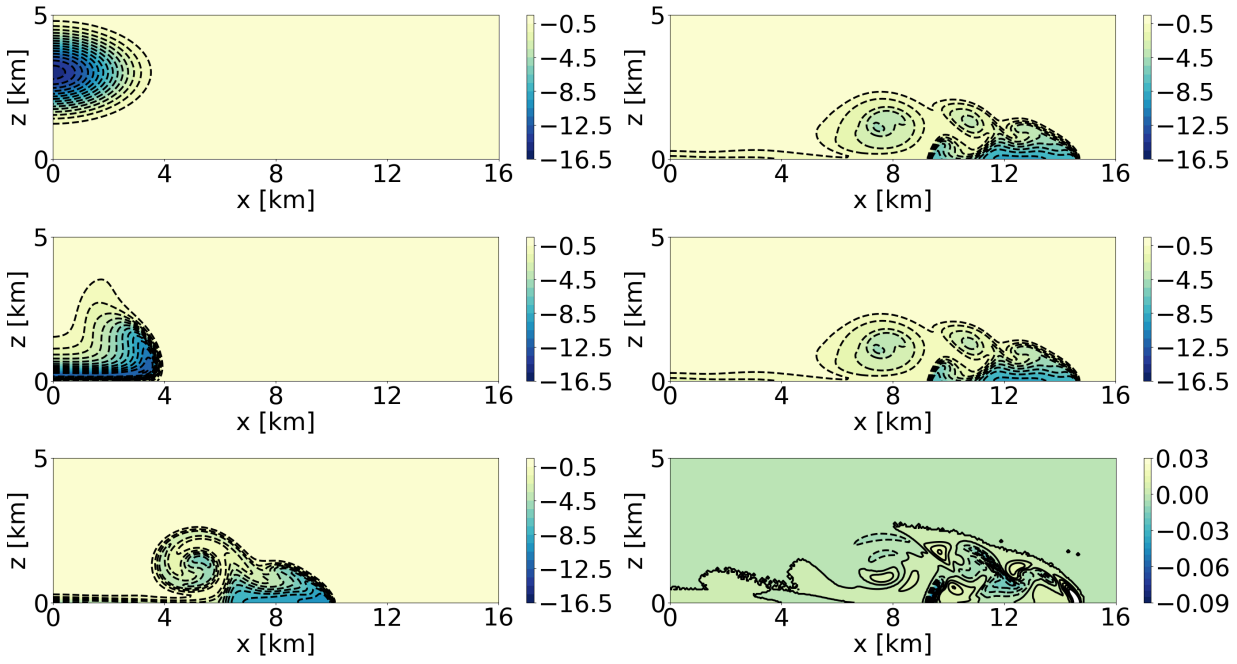

FIG. 2: Potential temperature perturbation for the density current test case of Straka et al. (1993) at spatial resolution $\Delta x = \Delta z = 50\,\mathrm{m}$ for the model with semi-implicit time stepping scheme at $t = 0$, 300, 600 s (left panel from top to bottom) and at $t = 900\,\mathrm{s}$ (upper right panel), a third-order Runge-Kutta time stepping scheme at $t = 900\,\mathrm{s}$ (middle right panel), and their difference (lower right panel). For the left and upper two right panels contours are in the range $[-16.5, 0.5]$ K with a contour interval of 1 K, and for the lower right panel $[-0.09, 0.03]$ K with a 0.005 K interval. Negative contours are dashed.

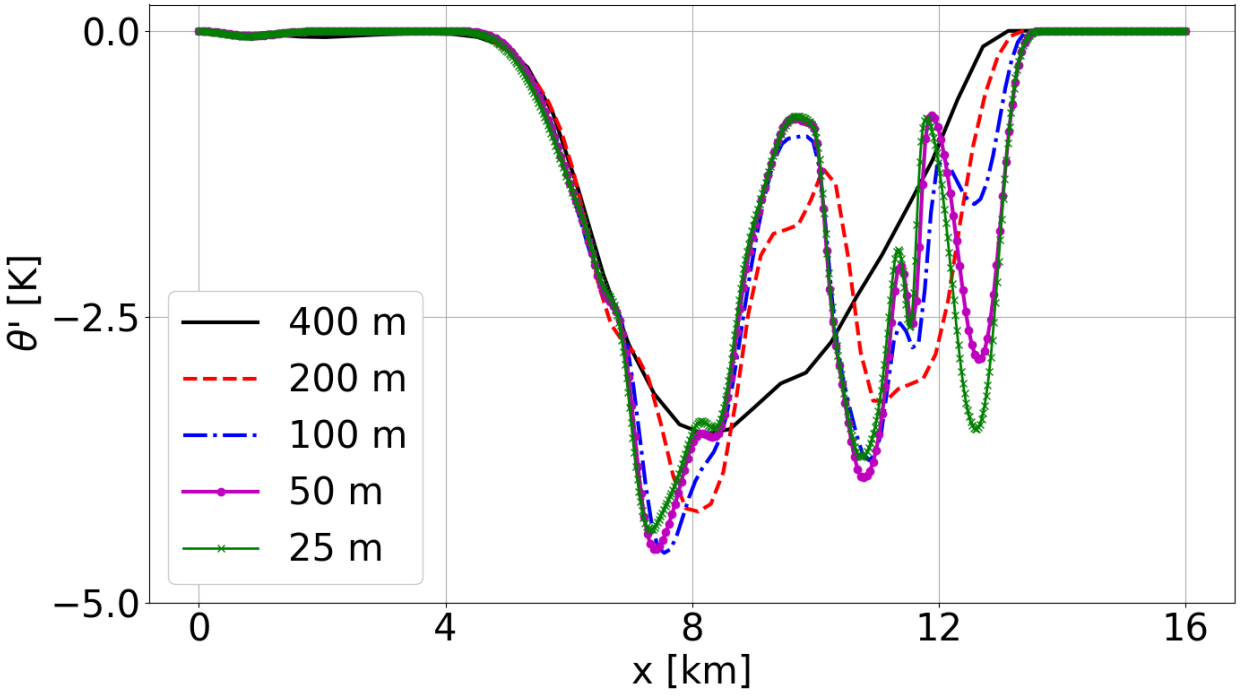

FIG. 3: Horizontal cross section of the potential temperature perturbation at height $z = 1200\,\mathrm{m}$ and final time $t = 900\,\mathrm{s}$ in the density current test case run with semi-implicit model for the following spatial resolution: 400 m (black solid), 200 m (red dashed), 100 m (blue dashed-dotted), 50 m (solid with dots), 25 m (green solid with crosses).

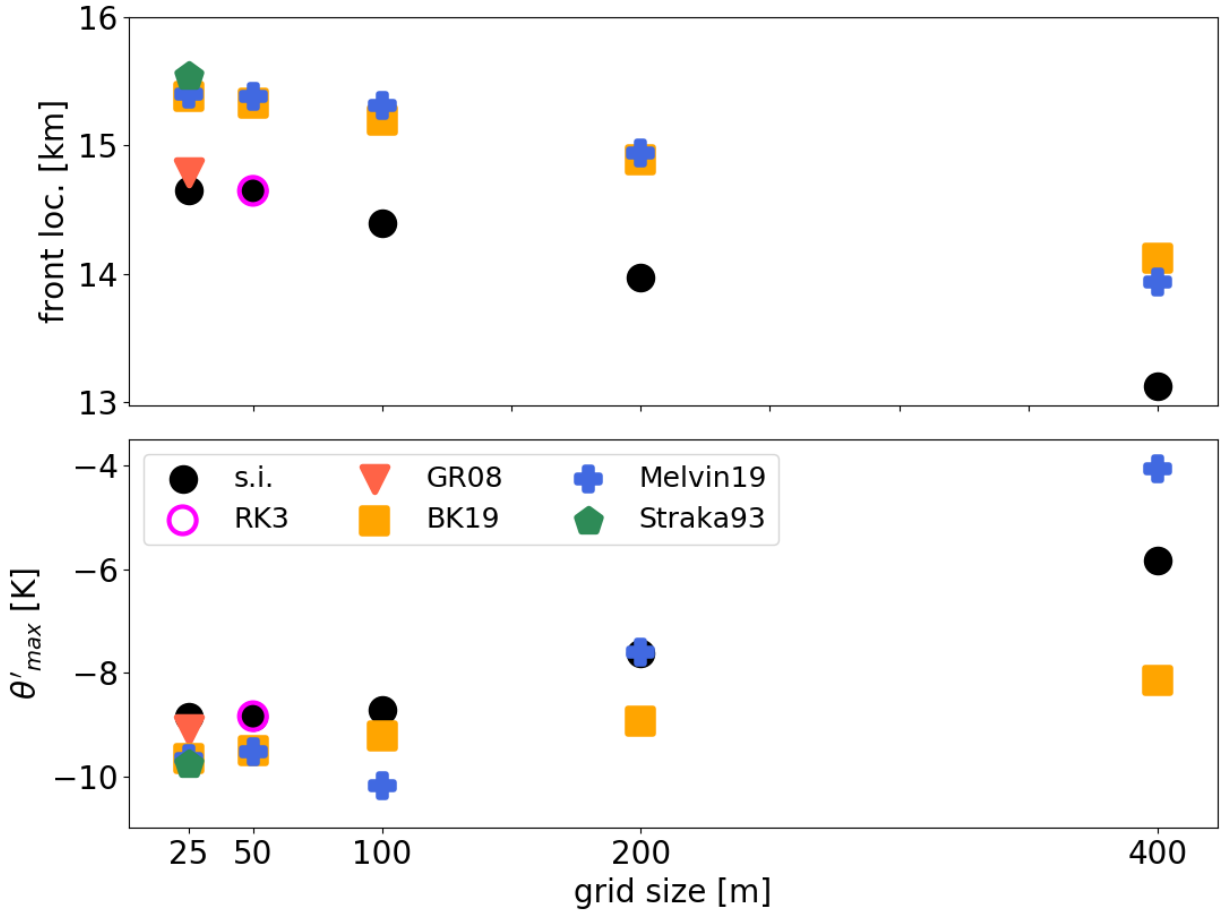

FIG. 4: Front location (i.e., the 1 K value of potential temperature perturbation, upper panel), and maximum potential temperature perturbation (lower panel) at final time $t = 900$ s in the density current test case run with semi-implicit time stepping scheme (s.i., black) and a third-order Runge-Kutta scheme (RK3, magenta). (i.e., Giraldo and Restelli (2008) (GR08, orange), Benacchio and Klein (2019) (BK19, yellow), and Melvin et al. (2019) (Melvin19, blue), Straka et al. (1993) (Straka93, green)).

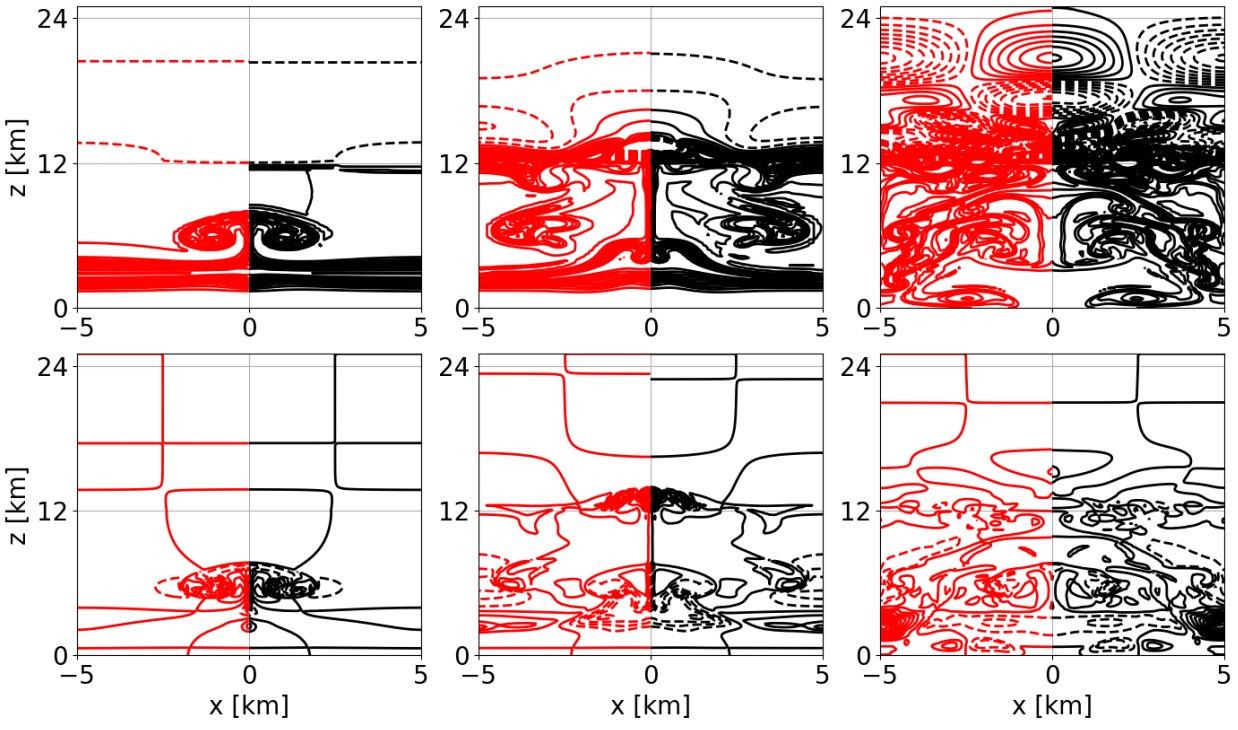

FIG. 5: Potential temperature (upper panel) and vertical momentum ρw (lower panel) for the heated profile with a local hot spot test case at spatial resolution $\Delta x = \Delta z = 125\,\mathrm{m}$ for the model with semi-implicit time stepping scheme (black contours) and a third-order Runge-Kutta time stepping scheme (red contours) at $t = 600\,\mathrm{s}$, $1200\,\mathrm{s}$, $1800\,\mathrm{s}$ (from left to right), respectively. For the potential temperature the contours are in the range $[-15, 7]$ K with a contour interval of $0.5\,\mathrm{K}$, and for the vertical momentum $[-0.2, 0.32]$ K with a $0.02\,\mathrm{K}$ interval. Negative contours are dashed.

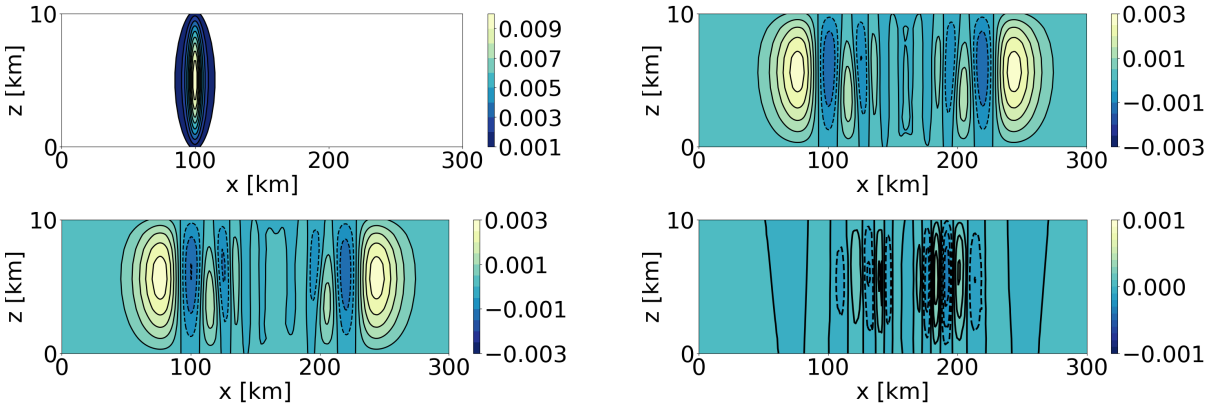

FIG. 6: Potential temperature perturbation for the non-hydrostatic IGW test case of Skamarock and Klemp (1994) at spatial resolution $\Delta x = \Delta z = 1\,\mathrm{km}$ for the model with semi-implicit time stepping scheme at initial time (upper left panel) and $t = 3000\,\mathrm{s}$ (upper right panel), a third-order Runge-Kutta time stepping scheme at $t = 3000\,\mathrm{s}$ (lower left panel), and their difference (lower right panel). For the initial data the contours are in the range $[0.001, 0.01]$ K with a contour interval of $0.001\,\mathrm{K}$, at $t = 3000\,\mathrm{s}$ $[-0.003, 0.003]$ K with a $5 \times 10^{-4}\,\mathrm{K}$ interval and for their difference $[-0.001, 0.001]$ K with a $1 \times 10^{-4}\,\mathrm{K}$ interval. Negative contours are dashed.

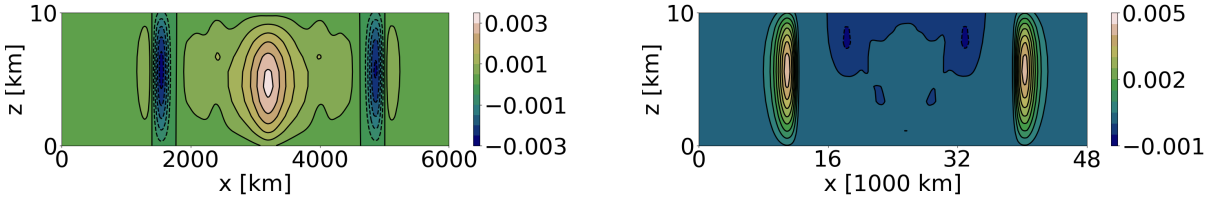

FIG. 7: Potential temperature perturbation for the hydrostatic IGW test case of Skamarock and Klemp (1994) at spatial resolution $\Delta x = 20\,\text{km}$, $\Delta z = 1\,\text{km}$ and final time $t = 60\,000\,\text{s}$ (left panel) and the planetary-scale gravity wave test of Benacchio and Klein (2019) at spatial resolution $\Delta x = 160\,\text{km}$, $\Delta z = 1\,\text{km}$ and final time $t = 480\,000\,\text{s}$ (right panel). For the hydrostatic IGW test case the contours are in the range $[-0.003, 0.0035]$ K with a contour interval of $5 \times 10^{-4}\,\text{K}$, and for the planetary-scale gravity wave test $[-0.001, 0.005]$ K with a $5 \times 10^{-4}\,\text{K}$ interval. Negative contours are dashed.

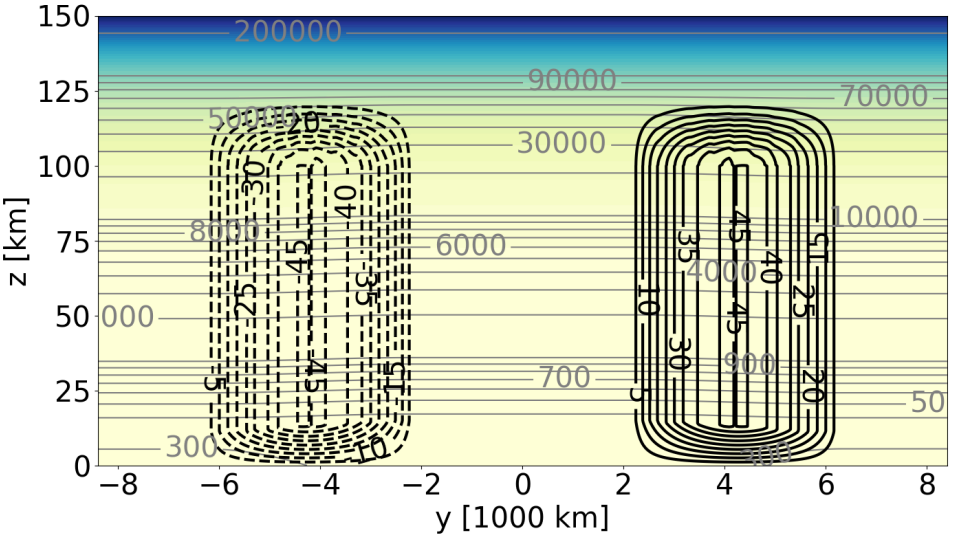

FIG. 8: Zonal mean of the initial conditions for the baroclinic wave life cycle. The black contours indicate the zonal wind [$\mathrm{m\,s^{-1}}$], the color shading and grey contours denote the potential temperature [K]. Negative contours are dashed.

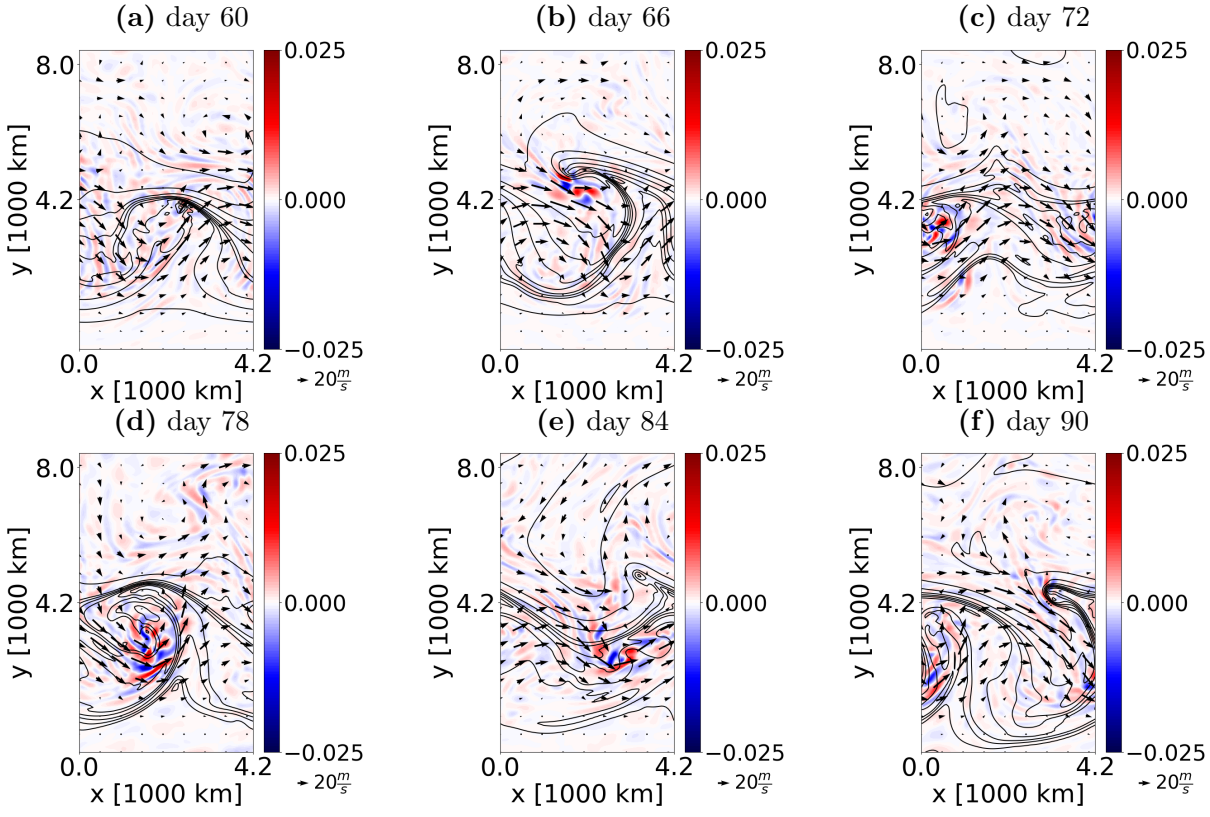

FIG. 9: Horizontal cross sections of the potential temperature [K] at $z = 250\,\mathrm{m}$ (contours), the horizontal wind speed [$\mathrm{m\,s^{-1}}$] at $z = 11.25\,\mathrm{km}$ (barbs) and the filtered (i.e., with horizontal scales less than 1000km) horizontal velocity divergence [$10^{-3}\,\mathrm{s^{-1}}$] at $z = 11.25\,\mathrm{km}$ (colors) on days 60, 66, 72, 78, 84, and 90 at 0000 UTC, respectively. The contour interval for the potential temperature is 3 K.

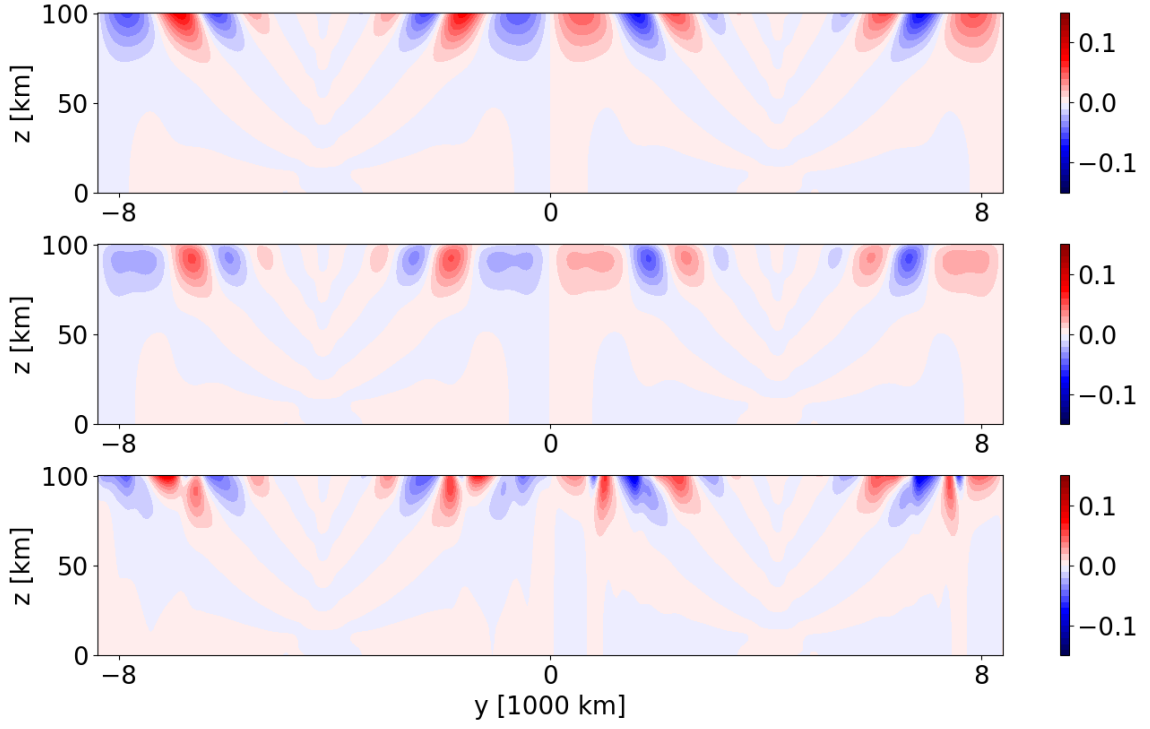

FIG. 10: Zonal average of the vertical velocity $[\mathrm{m\,s^{-1}}]$ for the model with semi-implicit time stepping scheme using a variable time step size (upper panel), using a constant time step size of $\Delta t = 2.28\,\mathrm{s}$ (middle panel) and a third-order Runge-Kutta time stepping scheme (lower panel) at $t = 2.5\,\mathrm{h}$.

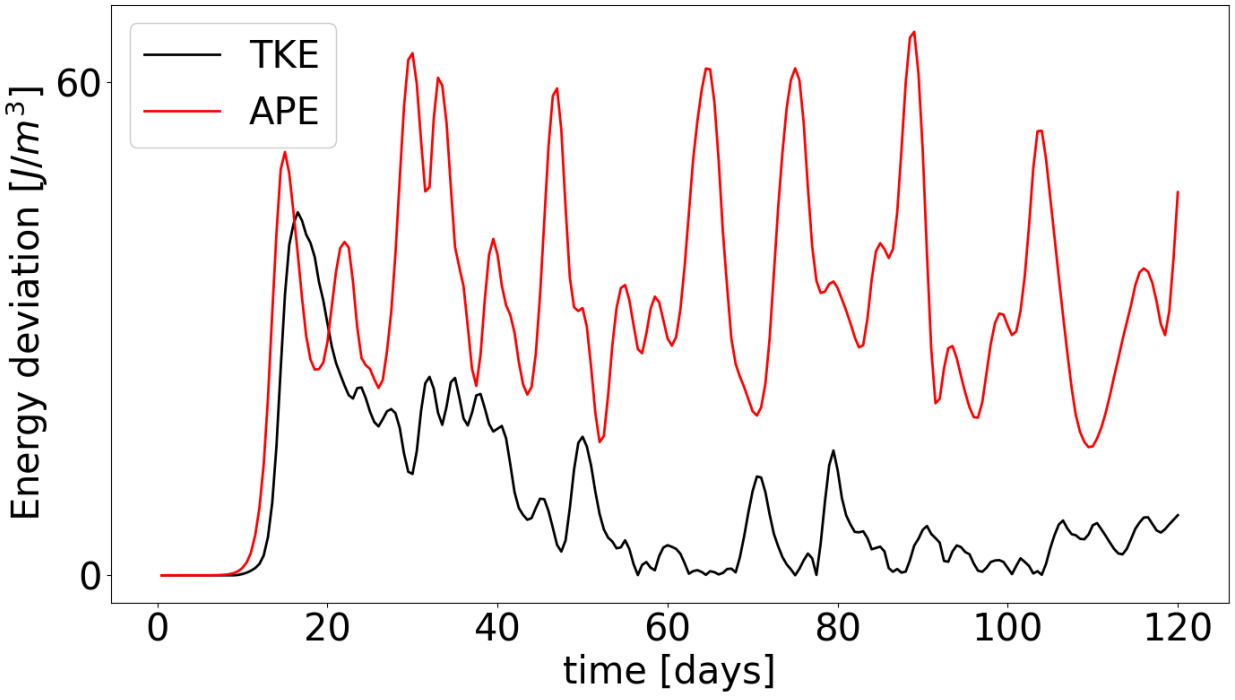

FIG. 11: Time evolution of deviations of the total kinetic energy (TKE, black) and the available potential energy (APE, red) from the corresponding initial values estimated at time $t = 0\,\mathrm{s}$.

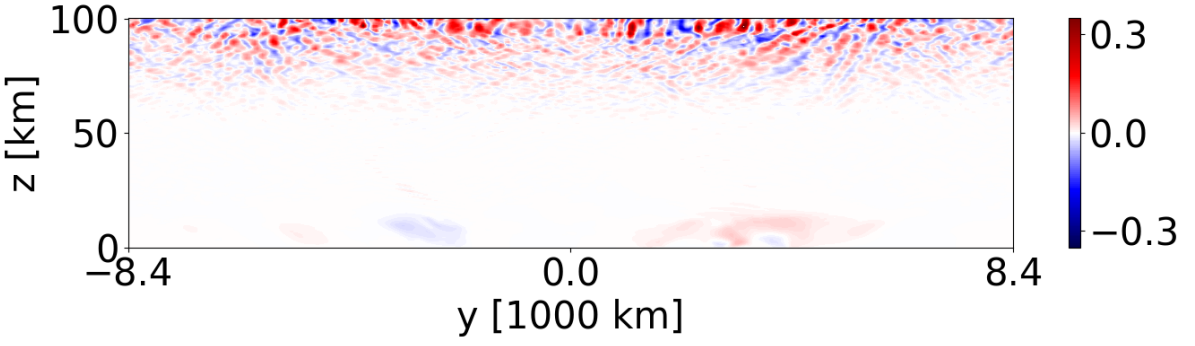

FIG. 12: Vertical cross section of the vertical wind perturbation [$\mathrm{m\,s^{-1}}$] at $x = 2100\,\mathrm{km}$ on day 120 at 0000 UTC.

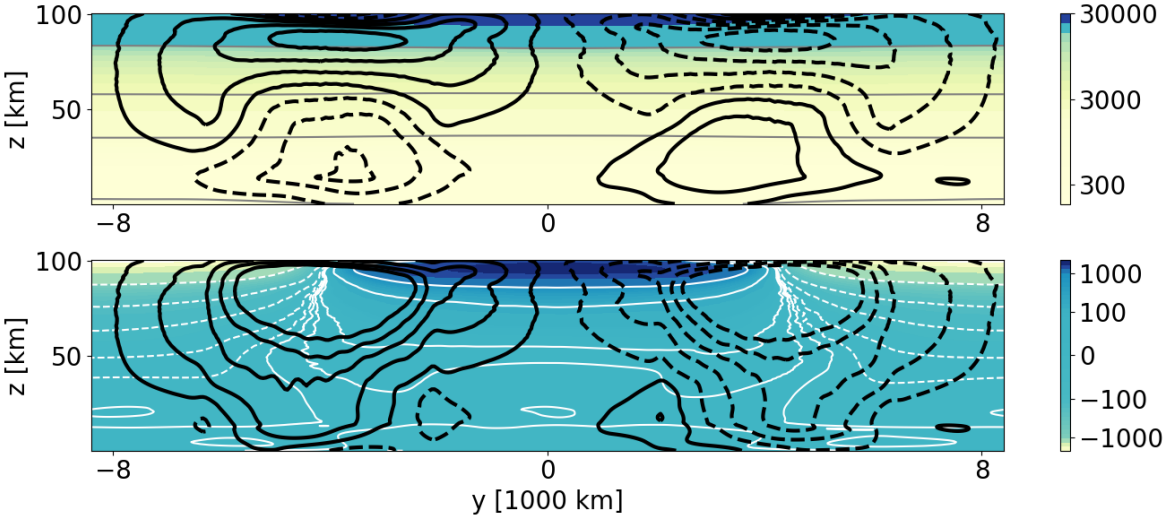

FIG. 13: Zonal mean of the zonal wind $[\mathrm{m\,s^{-1}}]$ (black contours in the range $[-45, 45]$ m s^{-1} with a contour interval of $10\,\mathrm{m\,s^{-1}}$) and potential temperature [K] (colors, grey contours in the range $[300, 10^5]$ K and white contours in the range $[-10^3, 10^3]$ K) averaged in time over days 60 – 120 at (upper panel), respectively, and their difference to the initial ambient state (i.e., $\langle u \rangle - u_{eq}$ and $\langle \theta \rangle - \theta_{eq}$) (lower panel). Negative contours are dashed.

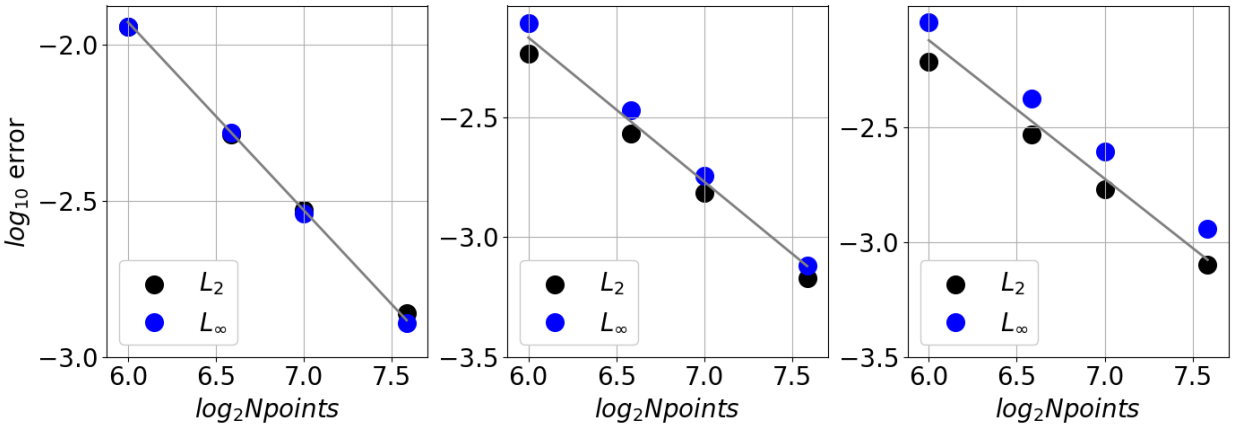

FIG. 14: Convergence study for the density (left), zonal (middle) and meridional velocity (right) in the travelling rotating smooth vortex test case of Kadioglu et al. (2008). Errors of the computed solutions with a horizontal grid spacing of $N \times N$ grid points at time $t =$ 1 s with respect to initial data in the L_2 and L_∞ norm. The grey line denotes the quadratic slope.

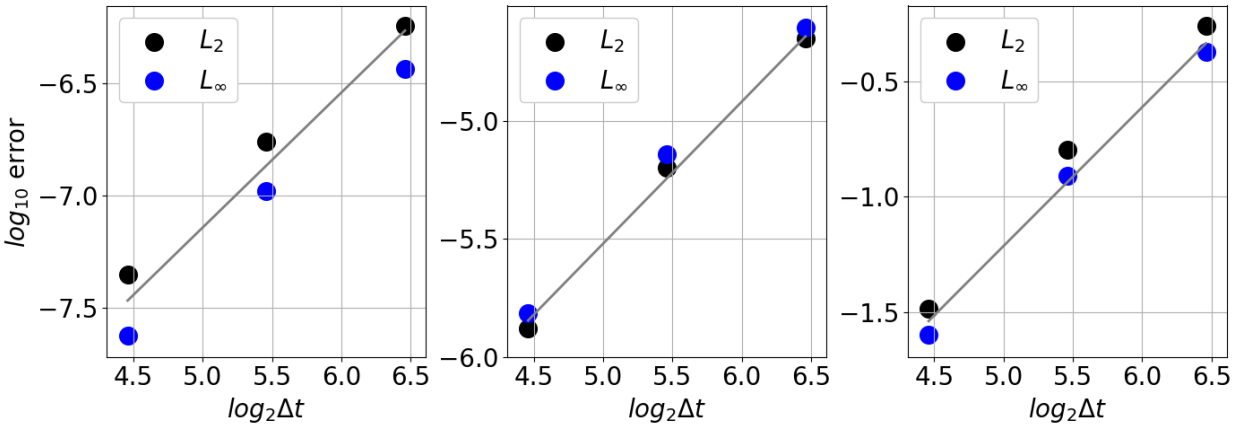

FIG. 15: Convergence study for the density (left), zonal (middle) and vertical velocity (right) in the non-hydrostatic IGW test case of Skamarock and Klemp (1994). Errors of the computed solutions with descresing $\Delta t = \text{const.}$ at time $t = 3000\,\text{s}$ with respect to a solution computed with $\Delta t = 11\,\text{s}$ in the L_2 and L_∞ norm. The grey line denotes the quadratic slope.